

ESD RECORD COPY

RETURN TO
SCIENTIFIC & TECHNICAL INFORMATION DIVISION
(ESTI BUILDING 121)

ESD ACCESSION LIST

ESTI Call No. AL 55954

Copy No. 1 of 2 cys.

ESD TR-67-162
ESTI FILE COPY

1

Solid State Research

1967

Prepared under Electronic Systems Division Contract AF 19(628)-5167 by

Lincoln Laboratory

MASSACHUSETTS INSTITUTE OF TECHNOLOGY

Lexington, Massachusetts



A100651065

The work reported in this document was performed at Lincoln Laboratory, a center for research operated by Massachusetts Institute of Technology, with the support of the U.S. Air Force under Contract AF 19(628)-5167.

This report may be reproduced to satisfy needs of U.S. Government agencies.

Distribution of this document is unlimited.

Non-Lincoln Recipients

PLEASE DO NOT RETURN

Permission is given to destroy this document
when it is no longer needed.

1

Solid State Research

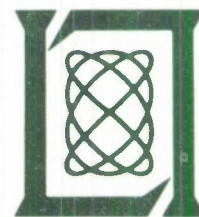
1967

Issued 4 April 1967

Lincoln Laboratory

MASSACHUSETTS INSTITUTE OF TECHNOLOGY

Lexington, Massachusetts



ABSTRACT

This report covers in detail the solid state research work at Lincoln Laboratory for the period 1 November 1966 through 31 January 1967. The topics covered are Solid State Device Research, Optical Techniques and Devices, Materials Research, and Physics of Solids.

Accepted for the Air Force
Franklin C. Hudson
Chief, Lincoln Laboratory Office

INTRODUCTION

I. SOLID STATE DEVICE RESEARCH

Electron beam excitation of CdS crystals grown in an atmosphere of excess Cd has resulted in laser emission near 4900 Å with 350 W of peak output power and 26.5-percent overall (35-percent internal) power efficiency at temperatures as high as 110°K . These values of power and efficiency represent more than an order-of-magnitude improvement over previously reported results. Laser action was observed, although at considerably reduced levels of power and efficiency, at temperatures up to 250°K . By using liquid helium as a coolant, an average output power of about 0.5 W could be maintained. Liquid nitrogen cooled samples produced up to 0.2 W of average power. The high performance of these new lasers appears to be due to increased crystal uniformity and to the introduction or enhancement of highly efficient radiative transitions, both of which result from the Cd-rich growth conditions.

Infrared photovoltaic response and a quantum efficiency of up to 25 percent have been observed at liquid nitrogen temperature in large area, InSb, metal-oxide-semiconductor structures. These structures consist of an InSb sample on which a 500-Å oxide layer was formed on one surface. A 100-Å thick semitransparent nickel film was then deposited on the oxide layer, and the infrared radiation was incident on the InSb through the film and the oxide layer. Spectral measurements indicate that the photoresponse is due to the generation of electron-hole pairs in a depletion region of the n-type InSb at the InSb-oxide interface. Pulsed current measurements yield a clear diode characteristic, and the overall results are equivalent to what one would expect to obtain from a photodiode in series with a MOS capacitor.

Single crystals of $\text{Pb}_{1-x}\text{Sn}_x\text{Te}$ alloys have been prepared by the Bridgman technique and by the vapor growth process. The overall results indicate that very large single crystals of a predetermined composition can be grown with a high degree of homogeneity by the Bridgman technique. However, these crystals possess high carrier concentrations, and must be annealed before useful devices can be fabricated from them.

$\text{Pb}_{1-x}\text{Sn}_x\text{Te}$ crystals were also vapor grown at various temperatures between 700° and 825°C . For $0.16 \leq x \leq 0.20$, p-type crystals were grown using metal-saturated source powders. An n-type skin, which is believed to form because of the preferential loss of Te (and probably Sn) from the surface during the cooling process, was observed on the crystals. For $x \leq 0.10$, only n-type crystals were grown from metal-saturated sources.

Gunn oscillation waveforms which are consistent with the electric-field-controlled differential negative resistivity of the transferred-electron model have been studied in CdTe. However, a current runaway process has also been observed which competes with the Gunn effect. During the runaway, band-gap radiation ($\sim 9000\text{ Å}$) is emitted in filaments reaching

Introduction

from one contact to the other. These latter effects are characteristic of a current-density-controlled differential negative resistivity.

II. OPTICAL TECHNIQUES AND DEVICES

Further measurements of heterodyne sensitivity have been made at $10.6\mu\text{m}$ using Cu-doped Ge detectors. The results are now in excellent agreement with the theoretically predicted value of $2h\nu B/\eta$ for the minimum detectable power, where B is the bandwidth and η is the quantum efficiency.

Preliminary measurements have established the feasibility of $\text{Pb}_x\text{Sn}_{1-x}\text{Te}$ as a heterodyne detector for $10.6\mu\text{m}$ operating at liquid nitrogen temperature (77°K). Initial measurements have yielded sensitivities much poorer than theoretical values; however, modifications in the detector design are expected to improve the performance.

Two stable CO_2 laser oscillators have been successfully operated and their frequency stability measured by observation of the beat frequency. The short-term stability is of the order of 9 and 20 kHz for observation times of 0.03 and 1 sec, respectively.

Further measurements have been made on a sealed-off CO_2 laser to determine the processes presently limiting operating lifetime. Studies of optical emission, power output, and mass spectrum analyses as a function of lifetime indicate that the principal performance degradation is caused by conversion of the carbon dioxide to carbon monoxide and oxygen.

III. MATERIALS RESEARCH

A crystal puller has been developed for the Czochralski growth of single crystals from melts produced by the arc-melting technique. Use of this apparatus eliminates the difficulty of finding crucible materials suitable for high-temperature growth, since the melt is contained by a solid shell of the same substance, which is in contact with a water-cooled copper hearth.

Single crystals of MnI_2 , a compound with the CdI_2 layer structure, have been prepared by freezing from the melt and by condensation from the vapor phase. Both types of growth were obtained when helium gas was used to transport MnI_2 vapor through a resistance-heated quartz tube with a suitable temperature profile.

X-ray diffraction and superconducting transition measurements have been made on InSb samples annealed at 65 kbars. The results show that at this pressure the transition from the room-temperature orthorhombic phase to the high-temperature InSb-III phase occurs between 175° and 225°C .

Single crystal films of $\text{Pb}_{1-x}\text{Sn}_x\text{Se}$ alloys with rocksalt structure have been deposited by evaporation on cleaved (100) faces of KCl substrates. The composition and temperature dependence of the energy gap, as determined from infrared transmission data, show that these alloys exhibit the inversion of conduction and valence bands recently proposed for the $\text{Pb}_{1-x}\text{Sn}_x\text{Te}$ alloys.

Magnetic susceptibility data, which have been obtained for MnYb_2S_4 , show that there is no appreciable magnetic interaction between the Mn^{2+} and Yb^{3+} ions. It has been established by x-ray diffraction measurements that this compound has a normal spinel structure with Mn^{2+} ions in the tetrahedral positions and Yb^{3+} ions in the octahedral positions.

IV. PHYSICS OF SOLIDS

Exciton fine structure in the interband magnetoabsorption spectrum of InSb has been observed and studied as a function of magnetic field. Some of the structure cannot be explained by the theory of Elliot and Loudon.

In the magneto-optical investigation of GaSe , measurements on vapor transport grown samples have yielded sharper lines as well as two additional new series of lines. Presumably, this improvement in spectra is due to the absence of strain in crystals prepared by this technique.

The analysis of the HgTe interband magnetoreflexion measurements has been completed. A least-squares fit of the data gives an energy gap $E_g = -0.283 \pm 0.001 \text{ eV}$ and a momentum matrix element parameter $E_p = 18.1 \pm 1.0 \text{ eV}$; these values are quite different from previous determinations which were not so direct.

The study of oscillations in the magnetoreflexion of arsenic continues. Some of the experimental results are in contradiction with the Lin-Falicov band model.

The Fourier expansion technique, previously applied to the calculation of the electronic energy bands and the dielectric constant of silicon and germanium, has now been used to obtain the lattice vibration spectrum for solids which crystallize in the diamond structure. Because of the availability of a large amount of experimental data, the band parameters for the phonon problem can be determined to a high degree of accuracy.

The zero field Cr^{53} nuclear resonance in the ferromagnetic state of the spinel, CdCr_2Se_4 , has been studied from liquid helium temperature to 115°K . Surprisingly, in the interval from 4.2°K to liquid nitrogen temperature the hyperfine field decreased linearly with temperature.

Calculation of the high-temperature expansion of the spin correlation function for the classical Heisenberg model, up to nine coefficients for the loose-packed lattices and to eight coefficients for the close-packed lattices, has been completed. The results are being applied to problems in magnetic ordering and neutron diffraction.

Resonant stimulated Raman scattering has been observed at $\sim 20^\circ\text{K}$ in a quartz sample cavity with plane, parallel end faces which formed a Fabry-Perot etalon. The measured Stokes line splittings indicate an index of refraction 10 to 20 percent larger than the usual index — presumably because of the nonlinear response of the material under high electric field.

The Raman spectra of trigonal, α -monoclinic, and amorphous selenium have been measured at room temperature with a YAG:Nd^{3+} laser. For the trigonal form mode, symmetries have been identified by polarization measurements, and the second-order spectrum has been explained in terms of two phonon transitions.

Introduction

A general technique for calculating Raman scattering from collective electron waves in solids has been developed, in which the coupling to the collective wave is expressed in terms of the thermally fluctuating vector and scalar potentials of the many-body system. The method can be used for longitudinal or transverse plasma waves and for mixed plasmon-phonon waves, and can also include the effect of magnetic fields.

By using a guiding-center distribution function, an expression for Landau damping of magnetoplasma waves has been derived for closed Fermi surfaces of arbitrary shape in the case where the cyclotron frequency is much greater than the collision frequency. The strength of the damping is found to be determined by the average over the cyclotron orbit of the power delivered by the wave to the resonant electrons.

CONTENTS

Abstract	iii
Introduction	v
Organization	xi
Reports by Authors Engaged in Solid State Research	xiii
 I. SOLID STATE DEVICE RESEARCH	 1
A. High Power and Efficiency in CdS Electron Beam Pumped Lasers	1
B. InSb MOS Infrared Detector	4
C. Crystal Growth, Composition Control, and Junction Formation in $Pb_{1-x}Sn_xTe$	6
1. Bridgman Crystal Growth	6
2. Isothermal Annealing	7
3. Vapor Growth	7
D. Negative Resistivity Effects in CdTe	8
 II. OPTICAL TECHNIQUES AND DEVICES	 11
A. Observation of Theoretically Predicted 10.6- μ m Heterodyne Sensitivity in Ge:Cu	11
B. Photovoltaic Heterodyne Detection of CO ₂ Laser Radiation in $Pb_xSn_{1-x}Te$	11
C. Stability Measurements of CO ₂ -N ₂ -He Lasers at 10.6- μ m Wavelength	13
D. CO ₂ 10.6- μ Laser	17
 III. MATERIALS RESEARCH	 21
A. Arc-Melting Furnace for Czochralski Growth of Single Crystals	21
B. Growth of MnI ₂ Single Crystals	24
C. High-Pressure Phase Diagram of InSb	24
D. Band Inversion in $Pb_{1-x}Sn_xSe$ Alloys	26
E. Magnetic Properties and Crystal Structure of MnYb ₂ S ₄	28
 IV. PHYSICS OF SOLIDS	 33
A. Electronic Band Structure	33
1. Exciton Fine Structure in Interband Magnetoabsorption of InSb	33
2. Magneto-Optical Studies on Vapor Transport Grown GaSe at 1.5 °K	33
3. Interband Magnetoreflexion and Band Structure of HgTe	37
4. Magnetoreflexion Experiments in Arsenic	38
5. Fourier Expansion of Phonon Dispersion Relations for Silicon and Germanium	39
B. Magnetism	39
1. NMR in Ferromagnetic Semiconductor CdCr ₂ Se ₄	39
2. High-Temperature Expansion of Spin Correlation Function for Classical Heisenberg Model	40
C. Scattering Experiments with Lasers	41
1. Resonant Stimulated Raman Scattering	41
2. Raman Spectra of Trigonal, α -Monoclinic, and Amorphous Selenium	41

ORGANIZATION

SOLID STATE DIVISION

A. L. McWhorter, *Head*
P. E. Tannenwald, *Associate Head*
M. J. Hudson, *Assistant*
E. P. Warekois
D. T. Stevenson*

SOLID STATE THEORY

H. J. Zeiger, *Leader*
M. M. Litvak, *Assistant Leader*

Argyres, P. N.	Larsen, D. M.
Chinn, S. R. [†]	Melanson, G. S., Jr.
Dresselhaus, G. F.	Palm, B. J.*
Hanus, J. G. C.	Stanley, H. E.*
Kaplan, T. A.	Trent, P. H.
Kelley, P. L.	Van Zandt, L. L.
Kleiner, W. H.	

OPTICS AND INFRARED

R. H. Kingston, *Leader*
R. J. Keyes, *Assistant Leader*

Bates, D. H.	McPhie, J. M.
Bostick, H. A.	Quist, T. M.
Carbone, R. J.	Sullivan, F. M.
Dennis, J. H.	Teich, M. C.
Freed, C.	Zimmerman, M. D.
Longaker, P. R.	

ELECTRONIC MATERIALS

J. B. Goodenough, *Leader*
J. M. Honig, *Associate Leader*
A. J. Strauss, *Assistant Leader*

Anderson, C. H., Jr.	Kafalas, J. A.
Andrews, H. I. [†]	LaFleur, W. J.
Arnott, R. J.	Lavine, M. C.*
Banus, M. D.	Longo, J. M.
Batson, D.	O'Connor, J. R.
Brebrick, R. F., Jr.	Owens, E. B.
Button, M. J.	Plonko, M. C.
Delaney, E. J.	Pollard, E. R. [†]
England, R. E.	Racchah, P. M.
Fahey, R. E.	Reed, T. B.
Farrell, L. B.	Roddy, J. T.
Ferretti, A.	Searles, I. H.
Finn, M. C.	Sohn, J. B.
Hilsenrath, S.	Soracco, D. J.
Iseler, G. W.	Steininger, J. A.

SOLID STATE PHYSICS

J. G. Mavroides, *Leader*
G. B. Wright, *Assistant Leader*

Burke, J. W.	Mastromattei, E. L.
Carman, R. L.*	Menyuk, N.
Dickey, D. H.	Murphy, H. C.
Dresselhaus, M. S.	Nill, K. W.
Dwight, K., Jr.	Parker, C. D.
Feinleib, J.	Perry, F. H.
Feldman, B.	Scouler, W. J.
Fulton, M. J.	Stickler, J. J. [†]
Groves, S. H.	Strahn, N. D. [†]
Johnson, E. J.	Thaxter, J. B.
Kernan, W. C.	Weber, R.
Kolesar, D. F.	Weinberg, D. L.
Krag, W. E.	

APPLIED PHYSICS

J. O. Dimmock, *Leader*
T. C. Harman, *Assistant Leader*
I. Melngailis, *Assistant Leader*

Butler, J. F.	Finne, P. C.	Lindley, W. T.	Phelan, R. J., Jr.
Calawa, A. R.	Foyt, A. G.	Mooradian, A.	Stella, J. A.
Carter, F. B.	Halpern, J.	Oliver, M. [†]	Ward, J. H. R., III
Caswell, F. H.	Hinkley, E. D.	Paladino, A. E.	Wolfe, C. M.
Clough, T. F.	Hurwitz, C. E.	Palermo, J. S.	Youtz, P.
Donaldson, P. L.			

* Part Time

[†] Research Assistant

REPORTS BY AUTHORS ENGAGED IN SOLID STATE RESEARCH

15 November 1966 through 15 February 1967

PUBLISHED REPORTS

Journal Articles*

JA No.

2652	Electron Recombination in Laser-Produced Hydrogen Plasma	M. M. Litvak D. F. Edwards	J. Appl. Phys. <u>37</u> , 4462 (1966)
2736	The Augmented Plane Wave Method and the Electronic Properties of Rare-Earth Metals	A. J. Freeman [†] J. O. Dimmock R. E. Watson [†]	<u>Theory of Atoms, Molecules and Solids</u> (Academic Press, New York, 1966)
2857	Unusual Crystal-Field Energy Levels and Efficient Laser Properties of YVO ₄ :Nd	J. R. O'Connor	Appl. Phys. Letters <u>9</u> , 407 (1966)
2879	Electro-Optic Effect in Trigonal Selenium at 10.6 μ m	M. C. Teich T. A. Kaplan	IEEE J. Quant. Electron. <u>QE-2</u> , 702 (1966)
2886	Stimulated Brillouin and Raman Scattering in Quartz at 2.1 to 293° Kelvin	P. E. Tannenwald J. B. Thaxter	Science <u>154</u> , 1319 (1966)
2889	Stimulated Four-Photon Interaction and Its Influence on Stimulated Rayleigh-Wing Scattering	R. Y. Chiao [†] P. L. Kelley [†] E. Garmire [†]	Phys. Rev. Letters <u>17</u> , 1158 (1966)
2912	Optimum Heterodyne Detection at 10.6 μ m in Photoconductive Ge:Cu	M. C. Teich R. J. Keyes R. H. Kingston	Appl. Phys. Letters <u>9</u> , 357 (1966)
2937	Donor Level Associated with (100) Conduction Band in S-Doped GaSb	B. B. Kosicki [†] W. Paul [†] A. J. Strauss G. W. Iseler	Phys. Rev. Letters <u>17</u> , 1175 (1966)
2942	Observation of Degenerate Stimulated Four-Photon Interaction and Four-Wave Parametric Amplification	R. L. Carman R. Y. Chiao [†] P. L. Kelley	Phys. Rev. Letters <u>17</u> , 1281 (1966)

* Reprints available.

[†] Author not at Lincoln Laboratory.

Reports

MS No.

- | | | | |
|------|--|--|---|
| 1394 | Magneto-Optical Effects in Solids | G. F. Dresselhaus
M. S. Dresselhaus | Estratto Rend. E. Fermi School <u>34</u> , 198 (1966) |
| 1554 | Spectroscopic Studies of Laser-Produced Hydrogen Plasma | M. M. Litvak
D. F. Edwards | IEEE J. Quant. Electron. <u>QE-2</u> , 486 (1966) |
| 1558 | Possibility of Self-Focusing Due to Intensity Dependent Anomalous Dispersion | A. Javan*
P. L. Kelley | IEEE J. Quant. Electron. <u>QE-2</u> , 470 (1966) |
| 1577 | Single-Crystal Growth and Electrical Transport Properties of the Spinel MgV_2O_4 | A. Ferretti
D. B. Rogers* | J. Phys. Chem. Solids Suppl. <u>E9</u> , 471 (1967) |
| 1608 | Oscillatory Magneto-Absorption in the Direct Transition in the Layer Compound Gallium Selenide at 1.50°K | J. Halpern | J. Phys. Soc. Japan <u>21S</u> , 180 (1966) |
| 1609 | Polaron Induced Anomalies in InSb | D. M. Larsen
E. J. Johnson | J. Phys. Soc. Japan <u>21S</u> , 443 (1966) |
| 1610 | Sulfur Donors in Silicon: Infrared Transitions and the Effects of Calibrated Uniaxial Stress | W. E. Krag
W. H. Kleiner
H. J. Zeiger
S. Fischler | J. Phys. Soc. Japan <u>21S</u> , 230 (1966) |
| 1611 | Magneto-Piezo-Optical Experiments in Semiconductors | J. G. Mavroides
M. S. Dresselhaus
R. L. Aggarwal*
G. F. Dresselhaus | J. Phys. Soc. Japan <u>21S</u> , 184 (1966) |
| 1612 | Magneto-Acoustic Effects in n-InSb at 9 GHz | K. W. Nill
A. L. McWhorter | J. Phys. Soc. Japan <u>21S</u> , 755 (1966) |
| 1814 | Characterization of d Electrons in Solids by Structure. 1. Localized vs Collective Electrons | J. B. Goodenough | Materials Res. Bull. <u>2</u> , 37 (1967) |

UNPUBLISHED REPORTS

Journal Articles

JA No.

- | | | | |
|------|---|---|-----------------------------------|
| 2811 | Superconducting Transition Temperature and Electronic Structure in the Pseudobinaries Nb_3Al-Nb_3Sn and Nb_3Sb-Nb_3Sb | F. J. Bachner
J. B. Goodenough
H. C. Gatos* | Accepted by J. Phys. Chem. Solids |
|------|---|---|-----------------------------------|

* Author not at Lincoln Laboratory.

JA No.			
2854A	The Structure of PbRuO_3 and Its Illustration of a Trap-Mediated Cation-Cation Bond	J. M. Longo P. M. Raccach J. B. Goodenough	Accepted by J. Chem. Phys.
2890	Interband Magneto-Optical Studies of Semiconductors and Semimetals	B. Lax* J. G. Mavroides	Accepted by Appl. Optics
2891	New Phase Transformation in InSb at High Pressure and High Temperature	M. D. Banus M. C. Lavine	Accepted by J. Appl. Phys.
2918	Semiconductor-to-Metal Transitions in Transition Metal Compounds	D. Adler* J. Feinleib H. Brooks* W. Paul*	Accepted by Phys. Rev.
2920	Semiconductor-to-Metal Transition in V_2O_3	J. Feinleib W. Paul*	Accepted by Phys. Rev.
2921	On the Thermodynamic Properties of Several Solid Phases of the Compound InSb	A. K. Jena* M. B. Bever* M. D. Banus	Accepted by Trans. Met. Soc. AIME
2923	Diode Lasers of $\text{Pb}_{1-y}\text{Sn}_y\text{Se}$ and $\text{Pb}_{1-x}\text{Sn}_x\text{Te}$	J. F. Butler A. R. Calawa T. C. Harman	Accepted by Appl. Phys. Letters
2932	High Power and Efficiency in CdS Electron Beam Pumped Lasers	C. E. Hurwitz	Accepted by Appl. Phys. Letters
2941	Retrograde Solubility in n-Type PbS	A. J. Strauss	Accepted by Trans. Met. Soc. AIME
2946	InSb MOS Infrared Detector	R. J. Phelan, Jr. J. O. Dimmock	Accepted by Appl. Phys. Letters
2948	The Electrical Properties and Band Structure of Doped LaInO_3	D. B. Rogers* J. M. Honig J. B. Goodenough	Accepted by Materials Res. Bull.
2955	Photo and Thermal Effects in Compensated Zinc Doped Germanium	R. J. Keyes	Accepted by J. Appl. Phys.
2962	The GaAs-InSb Graded-Gap Heterojunction	E. D. Hinkley R. H. Rediker	Accepted by Solid-State Electron.

* Author not at Lincoln Laboratory.

Reports

JA No.

2963A	Inversion of Conduction and Valence Bands in $\text{Pb}_{1-x}\text{Sn}_x\text{Se}$ Alloys	A. J. Strauss	Accepted by Phys. Rev.
2967	Landau Damping of Magnetoplasma Waves for General Closed Fermi Surfaces	A. L. McWhorter J. N. Walpole	Accepted by Phys. Rev.
2968	Nonlocal Effects in Low-Field Helicon Propagation in PbTe	J. N. Walpole A. L. McWhorter	Accepted by Phys. Rev.

MS No.

1746	Dependence of the Critical Properties of Heisenberg Magnets on Spin and Lattice	H. E. Stanley T. A. Kaplan	Accepted by J. Appl. Phys.
1747	Possibility of a Phase Transition for the Two-Dimensional Heisenberg Ferromagnet	H. E. Stanley T. A. Kaplan	Accepted by J. Appl. Phys.
1791	Spontaneous Band Magnetism	J. B. Goodenough	Accepted by J. Appl. Phys.
1815	Experimental Techniques with General Applicability for the Study of Magnetic Phenomena	K. Dwight	Accepted by J. Appl. Phys.

Meeting Speeches*

MS No.

1612A	Magnetoacoustic Effects and Ultrasonic Amplification in n-InSb at 9 GHz	K. W. Nill	Seminar, M.I.T., 21 November 1966
1661A	The Fourier Expansion for Electronic Energy Bands	G. F. Dresselhaus	Seminar, Ford Motor Scientific Research Laboratory, Dearborn, Michigan, 17 November 1966
1719C	Interstellar 18 cm OH Maser Emission	M. M. Litvak A. L. McWhorter M. E. Meeks† H. J. Zeiger	American Astronomical Society, Los Angeles, California, 27 - 30 December 1966
1719D	Interstellar OH Maser Emission	A. L. McWhorter	Seminar, M.I.T., 22 November 1966
1745A	Recent Results for the Heisenberg Model from High-Temperature Expansions	H. E. Stanley	Seminar, Yeshiva University, New York, 1 December 1966

*Titles of Meeting Speeches are listed for information only. No copies are available for distribution.

† Division 3.

MS No.			
1787A	Spin Waves in Paramagnetic Fermi Gases	L. L. Van Zandt	Seminar, United Aircraft, Hartford, Connecticut, 26 January 1967
1793	Observation of Polaron Effects on the Interband Magnetoabsorption of InSb	E. J. Johnson D. H. Dickey D. M. Larsen	American Physical Society, Nashville, Tennessee, 1 - 3 December 1966
1796	Landau Level Raman Scattering	P. L. Kelley G. B. Wright	
1797	Current-Modulated Magnetoreflexivity in InSb	J. Feinleib C. R. Pidgeon* S. H. Groves	
1798	The Raman Spectrum of Trigonal Selenium	A. Mooradian G. B. Wright	
1799	Current-Modulated Reflectance of Gold from 2-10 eV	W. J. Scouler	
1800	Stimulated Brillouin and Raman Scattering in Quartz at 2.1 to 293° Kelvin	P. E. Tannenwald J. B. Thaxter	
1801	The Raman Spectrum of GaS and GaSe	G. B. Wright A. Mooradian	
1821	Polaron Energy Spectrum	D. M. Larsen	American Physical Society, Stanford, California, 28 - 30 December 1966
1808	Magnetoreflexion Experiments in Arsenic	M. S. Maltz* S. Fischler M. S. Dresselhaus	
1809	Amplification of 9 GHz Ultrasonic Waves in n-InSb	K. W. Nill	
1818	Fourier Expansion for the Energy Bands in Silicon	M. S. Dresselhaus G. F. Dresselhaus	American Physical Society, New York, 30 January - 2 February 1967
1819	Raman Excitation of Collective Waves in Solids	A. L. McWhorter P. N. Argyres	
1820	High-Temperature Expansion of the Magnetic Susceptibility for the Classical Heisenberg Model	H. E. Stanley	
1885	Stimulated Four-Photon Interaction	R. L. Carman R. Y. Chiao* E. Garmire* P. L. Kelley	

* Author not at Lincoln Laboratory.

Reports

MS No.

1822	Recent Work on High Electric Field Effects in GaAs	A. G. Foyt	Seminar, Cornell University, 21 November 1966
1830	Metallic Properties of Certain Metal Oxides	J. M. Honig	Colloquium, Brown University, 5 January 1967
1838	Laser Principles and State-of-the-Art Crystal and Semiconductor Lasers	R. H. Kingston	American Association for the Advancement of Science, Washington, D.C., 30 December 1966
1839	Low Field Avalanche in n-CdTe	M. R. Oliver A. G. Foyt	Conference on Active Microwave Effects in Bulk Semiconductors, New York, 2 - 3 February 1967
1841	Recent Progress in Infrared Lasers and Detectors	J. O. Dimmock	Solid State Physics Colloquium, Washington, D.C., 5 January 1967
1842	Light-by-Light Scattering Due to Molecular Orientation	P. L. Kelley R. Y. Chiao*	Seminar, M.I.T., 16 December 1966
1843	Interstellar OH Maser Emission	H. J. Zeiger	Seminar, Northeastern University, 20 December 1966
1846	An Effective Hamiltonian for the Optical Properties of Si and Ge	G. F. Dresselhaus	Seminar, M.I.T., 6 January 1967
1857	Effective Mass Hamiltonian and the Dielectric Constant for Si and Ge	G. F. Dresselhaus M. S. Dresselhaus	} Winter Institute in Quantum Chemistry, Solid-State Physics, and Quantum Biology, Sanibel Island, Florida, 5 December 1966 - 21 January 1967
1859	Proof of the Virial Theorem for the Electron Gas	P. N. Argyres	
1871	Critical Phenomena in Heisenberg Models of Magnetism	H. E. Stanley	Colloquium, Brandeis University, 17 January 1967

* Author not at Lincoln Laboratory.

I. SOLID STATE DEVICE RESEARCH

A. HIGH POWER AND EFFICIENCY IN CdS ELECTRON BEAM PUMPED LASERS

Electron beam excitation of CdS crystals grown in an atmosphere of excess Cd has resulted in laser emission near 4900 Å with 350 W of peak output power and 26.5-percent overall (35-percent internal) power efficiency at temperatures as high as 110°K . These values of power and efficiency represent more than an order-of-magnitude improvement over previously reported results.¹ Laser action was observed, although at considerably reduced levels of power and efficiency, at temperatures up to 250°K . The high performance of these new lasers appears to be due to increased crystal uniformity and to the introduction or enhancement of highly efficient radiative transitions, both of which result from the Cd-rich growth conditions.

The thin CdS crystal platelets were grown[†] from CdS powder by vapor transport, in approximately 1-atm. pressure of Cd vapor. Rectangular laser samples, $0.5 \times 1.5\text{ mm}$ on a side, were cleaved from the $25\text{-}\mu$ thick platelets and mounted on the cold finger of a dewar with vacuum grease or pure indium solder. A high-reflectivity aluminum layer was evaporated on one of the $1.5\text{ mm} \times 25\text{ }\mu$ cleaved faces. The electron beam, 0.5 mm in diameter, was pulsed with 0.05- to $5\text{-}\mu\text{sec}$ pulses at repetition rates from 60 to 10,000 Hz.

Although laser emission was observed at incident electron energies as low as 11 keV, substantial output power and efficiency were obtained only for energies in excess of about 40 keV. This is probably due to the reduced influence of the surface and to the increase in active volume accompanying the deeper penetration of the higher energy electrons. With a 60-keV, 22-mA beam (the maximum available with the present apparatus), a peak power output of 350 W was obtained. The output power level remained essentially constant over the temperature range from 4.2° to 110°K , while the threshold current, which reached values as low as $50\text{ }\mu\text{A}$ at 4.2°K , rose slowly with increasing temperature, approximately doubling over this temperature interval. With further increase in temperature, however, the threshold current began to rise very rapidly, with a corresponding decrease in power output, until at 250°K the full 22-mA, 60-keV beam was required to reach the laser threshold. At 300°K , superlinearity of the spontaneous emission intensity as a function of beam current was observed at high currents, indicating that laser action could probably be achieved at room temperature with a more powerful electron beam. The wavelength of the laser emission peak increased from 4897 to 5185 Å at 250°K , corresponding to the decrease of the energy gap with temperature.²

By using liquid helium as a coolant, the full 350-W output could be sustained for a pulse width of up to $0.5\text{ }\mu\text{sec}$ and a repetition rate of up to 3 kHz, resulting in an average output power of about 0.5 W. Liquid nitrogen-cooled samples produced up to 0.2 W of average power. Limiting values for the pulse width and repetition rate were imposed by the instantaneous and average heating of the sample, respectively, as evidenced by the fact that reduced beam power input permitted higher duty cycles. Further, the samples mounted using indium solder achieved higher

[†] These platelets were grown by D.C. Reynolds of the Aerospace Research Laboratory, Wright-Patterson Air Force Base.

Section I

average power outputs than those mounted with vacuum grease, which has a much lower thermal conductivity.

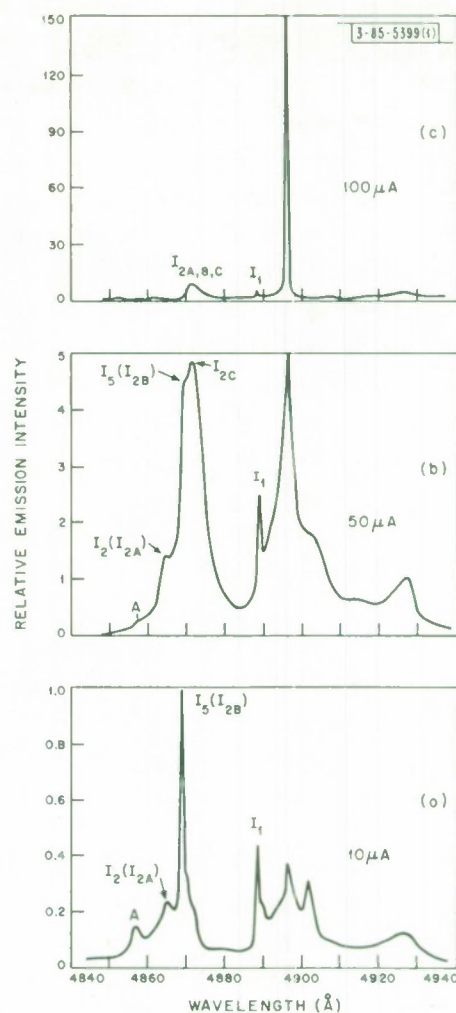
The overall power conversion efficiency of the lasers, computed from the above results, is 26.5 percent. From the data of Sternglass³ and Holliday and Sternglass,⁴ it can be determined that for 60-keV electrons incident on CdS (average atomic number 32) the fraction of electrons backscattered is 0.3 and that the mean fraction of the initial energy retained by these electrons is very nearly 0.6, with the result that about 18 percent of the incident power is lost by back-scattering. In addition, there is about 8-percent optical loss in the evaporated aluminum reflective coating⁵; hence, the internal power conversion efficiencies are at least 35 percent. From the limited experimental data^{6,7} and simple theoretical arguments^{8,9} concerning the mean energy required to create an electron-hole pair in CdS by electron bombardment, we can estimate that the maximum expected power conversion efficiency is of the order of 30 to 40 percent. This would indicate that the present CdS lasers have quantum efficiencies for electron-hole recombination of very nearly unity.

The effect of the Cd-rich growth atmosphere in inducing the observed high power and efficiency and low threshold in these CdS lasers appears to be twofold. Whereas previously reported samples exhibited laser action only in small localized filaments,¹ emission in the present lasers is uniform and continuous over large portions of the samples, the active area often being limited in dimension only by the size of the electron beam. This indicates that the cadmium overpressure during growth promotes a much more homogeneous crystal composition, which contributes significantly to the improved performance of the lasers. In addition, the laser emission in the present crystals results from two emission lines which have been introduced or at least greatly enhanced by the growth in excess Cd vapor. These lines appear at 4897 and 4902 Å, as seen in the typical spontaneous emission spectrum of Fig. I-1(a). Depending on the particular crystal being bombarded, the stimulated emission appears from one or the other of these lines, and sometimes from both simultaneously.

The rapid rise in intensity and spectral narrowing of the 4897-Å line as lasing is achieved is shown in Figs. I-1(b) and (c). The other designated lines in the spectra of Fig. I-1 are the more commonly observed CdS emission lines, most of which have been studied and at least tentatively identified by others as being due to recombination of various free and bound excitons.¹⁰ In particular, the I_1 line appears to result from the recombination of excitons bound to a neutral acceptor, which is probably a Cd vacancy, as evidenced by the fact that the I_1 line is suppressed by annealing CdS in a Cd atmosphere.¹¹ The relatively low intensity of the I_1 line compared with that of the I_5 (I_{2B}) line in the present samples indicates that crystal growth in a Cd overpressure has at least partially produced the same result.

In previous work, the author^{1,12} and others¹³ observed laser emission in CdS both from the I_1 line and at slightly lower energies, often at wavelengths nearly identical with those of the present results. The latter emission occurred within the acoustic phonon wing of the strong I_1 line, and consequently was attributed to recombination of the I_1 exciton with phonon cooperation. However, in light of the relative prominence of the two distinct lines at 4897 and 4902 Å from which laser emission occurs in the present samples, it appears likely that the transitions which produce these lines are quite separate and distinct from those responsible for the I_1 line. In support of

Fig. I-1(a-c). Emission spectra of CdS at 4.2°K excited by 50-keV electron beam for three values of beam current. Note relative intensity scales.



this conclusion, Reynolds and co-workers,¹⁴ using similarly grown Cd-rich crystals in which the I_1 line is almost totally absent, have observed in the vicinity of 4900 Å several prominent emission lines, one of which (located at 4895 Å) is often very intense. In all likelihood this is the same line that we observe at 4897 Å from which laser emission is obtained. Also in earlier work, Thomas and Hopfield¹⁵ noted lines around 2.53 eV (4900 Å) which were unrelated to the I_1 line.

One further observation which may prove to be of significance in identifying the laser transition can be seen in Figs. I-1(a) and (b). As the beam current is increased and the 4897-Å line begins to increase rapidly in intensity, a rather broad line at about 4871 Å also begins to increase in amplitude at nearly the same rate, until strongly stimulated emission appears to occur in the former line, at which point the latter line saturates in intensity. This 4871-Å line could be the I_{2C} line tentatively attributed by Handleman and Thomas¹¹ to an exciton bound to a donor level. The possible relationship between this line and the 4897-Å line remains to be investigated.

C. E. Hurwitz

Section I

B. InSb MOS INFRARED DETECTOR

We have observed infrared photovoltaic response with a high quantum efficiency in large area, InSb, metal-oxide-semiconductor structures. Spectral measurements indicate that the photoresponse is due to the generation of electron-hole pairs in the depletion region of the n-type InSb at the InSb-oxide interface. The photovoltaic response of diffused and grown p-n junctions of InSb has been studied extensively by other workers; these devices have been utilized as fast, sensitive, infrared detectors. In addition, there have been numerous reports on the enhanced photoconductivity of semiconductors subjected to oxidation¹⁶ as well as a study of the photovoltaic response from some metal-insulator-semiconductor structures.¹⁷ In the present work, the detector is formed without the use of the elevated temperatures of diffusion or the required control and processing of grown junctions. Furthermore, the thin oxide layer on the n-type InSb provides a coupling capacitance which is much larger than the junction capacitance and allows one to observe the large quantum efficiencies.

The structures studied consist of an InSb sample on which an oxide layer was formed on one surface by anodizing the InSb using a 0.1 N KOH solution.^{18,19} A semitransparent nickel film was then deposited on the oxide layer, and the infrared radiation was incident on the InSb through the film and the oxide layer. The anodization can easily be controlled to produce large-area uniform oxide layers. For these studies, the oxide film thickness was kept in the neighborhood of 500 Å. The evaporated nickel films were about 100 Å thick. Small opaque areas of gold were evaporated on the nickel to allow for spring contacts. The structure was mounted in vacuum with the InSb side attached to a liquid nitrogen-cooled heat sink.

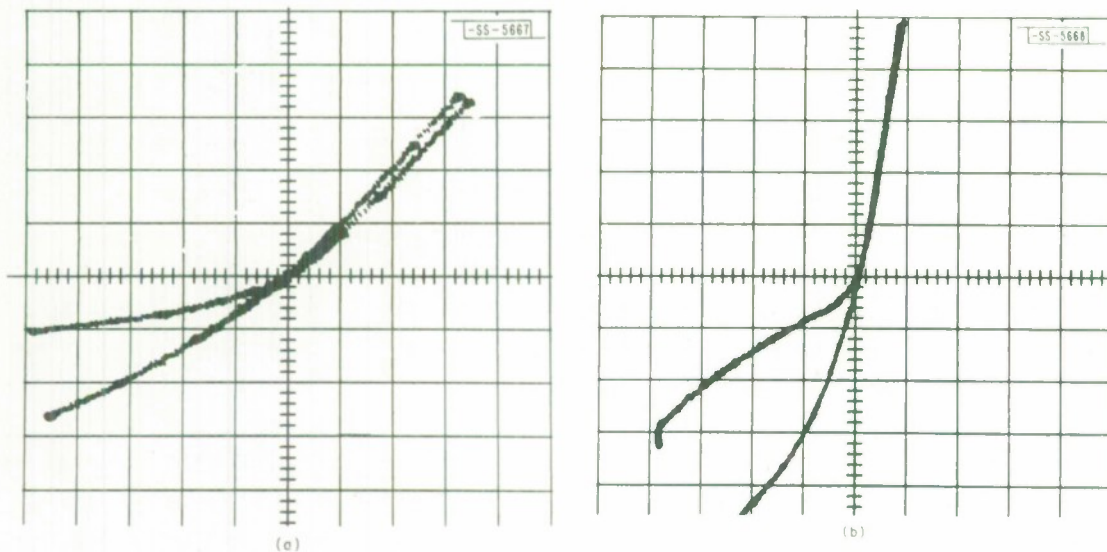


Fig.1-2. Current-voltage characteristics of InSb depletion region obtained by sampling a portion of 1- μ sec pulses. Upper curves in third quadrant correspond to an illumination with room radiation, and lower curves to illumination from a glabar source. Curves cross at origin. (a) Vertical scale is 1 mA/cm⁻¹, and horizontal scale is 0.05 V/cm⁻¹; (b) vertical scale is 1 mA/cm⁻¹, and horizontal scale is 0.25 V/cm⁻¹.

These devices have yielded a large infrared photovoltaic response at zero bias due to the production of electron-hole pairs in the InSb. The response is consistent with a model for the band curvature in the InSb near the oxide interface which for n-type bulk material yields a surface p-type inversion region. The surface inversion and accumulation of anodized InSb have been investigated elsewhere by studying the MOS structure capacitance as a function of applied bias.²⁰ In the present work, the diode characteristics were obtained by measuring the current vs voltage using short pulses with a low repetition rate. Pulse lengths of about 1 μ sec were used such that the current could be measured after the junction capacitance had charged, but before the oxide capacitor between the metal and semiconductor had charged by more than a few percent. A low repetition rate was chosen to allow the oxide capacitor to discharge completely between pulses.

Resulting current-voltage curves are shown in Figs. I-2(a) and (b) for a sample with a bulk n-type concentration of 1.0 to $1.2 \times 10^{14} \text{ cm}^{-3}$ and a Hall mobility greater than $7.0 \times 10^5 \text{ cm}^2/\text{V-sec}$. Two curves crossing at the origin are shown in each oscilloscope photograph: one with only background room radiation, the other with a constant global illumination. The results are equivalent to what one would expect to obtain from a photodiode in series with a capacitor. From the vertical displacement in the reverse bias region, a photon collection quantum efficiency of 25 percent was obtained. The quantum efficiency appears to be limited to this value simply by the reflection and losses in the semitransparent film and the reflectivity of the InSb. With no applied bias current, a photovoltage is developed which can be observed by using a voltmeter with a higher input impedance than the resistance of the oxide or by using a chopped light source. The photovoltaic response as a function of wavelength is shown in Fig. I-3. The response is given in units of D_λ^* , a common figure of merit for infrared detectors defined by

$$D_\lambda^* = \frac{V_S (A_D \Delta f)^{1/2}}{V_N P_\lambda}$$

where V_S is the rms signal voltage, V_N is the rms noise voltage, A_D is the detector area, Δf is the electronic bandwidth of the measuring apparatus, and P_λ is the incident power at the wavelength λ . The response curve in Fig. I-3 is characteristic of electron-hole pair excitation across

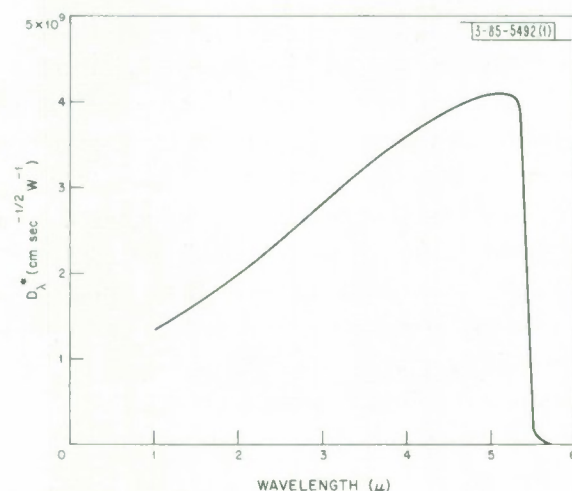


Fig. I-3. Detectivity D_λ^* as a function of wavelength.

Section I

the gap in InSb and extends to 5.4μ . The peak detectivity thus far obtained is $4 \times 10^9 \text{ cm/W-sec}^{1/2}$ for a device with an area of 0.1 cm^2 and a field of view of approximately $2\pi \text{ sr}$.

As mentioned above, the photovoltaic response observed in our MOS devices depends on the existence of a surface depletion region in the n-InSb. The exact cause of the band bending which brings about this depletion region has not been determined. Moreover, there is also considerable variation in the literature as to whether oxide surface states tend to bend the conduction and valence bands in InSb up or down.²⁰⁻²⁶ Our present work indicates a depletion region in n-type material, although we have not eliminated the possible conversion of the surface from n- to p-type due to room illumination. However, we have also used pyrolytic SiO_2 in place of the anodized film and again obtained a depletion region and the same high quantum efficiency. We have used an etch to restore the surface stoichiometry²⁷ before applying the oxide and obtained the same results. The n-type material with an extrinsic concentration of 10^{15} cm^{-3} yields the same spectral response, but p-type material of an extrinsic concentration of 10^{15} cm^{-3} did not yield a measurable long wavelength response at zero bias current. The p-type material did yield a photovoltaic response characteristic of the oxide.²² This response is limited to short wavelengths, is observed at room temperature, and, in contrast to the response of the depletion layer in the InSb, is optimized by chopping the light at low frequencies (the oxide response is shunted by the MOS capacitor while the InSb depletion layer response is in series with this capacitor).

Although we have not resolved the exact nature of the surface states in anodized InSb, we have found that the resulting structure may be used to form large-area MOS infrared detectors exhibiting a high quantum efficiency and a high detectivity. Since the depletion region is at the semiconductor surface, the absorption of light occurs in a high field region, thereby yielding high collection efficiencies. These results indicate that MOS structures of InSb, as well as other low-bandgap semiconductors, should be very useful as highly efficient infrared photovoltaic detectors.

R. J. Phelan, Jr.
J. O. Dimmock

C. CRYSTAL GROWTH, COMPOSITION CONTROL, AND JUNCTION FORMATION IN $\text{Pb}_{1-x}\text{Sn}_x\text{Te}$

1. Bridgman Crystal Growth

Single crystals of the PbSnTe alloys have been prepared by the Bridgman technique and by the vapor growth process. For the Bridgman-grown alloys with $x \leq 0.2$, electron microprobe analysis has shown that the surface of crystal slices cut perpendicular to the growth direction are homogeneous within the experimental error of the microprobe of ± 0.5 mole-percent SnTe. The compositional variation along the length L of a typical Bridgman crystal is: $x = 0.127$ for $L = 0$, to $x = 0.140$ for $L = 5 \text{ cm}$. The alloy composition and hole-carrier concentration for the first-to-freeze alloys are given in Table I-1. It is concluded that very large single crystals of a predetermined composition can be grown with a high degree of homogeneity by the Bridgman technique. However, these crystals possess high carrier concentrations, and must be annealed to reduce this concentration before useful devices can be fabricated from them.

TABLE I-1 LIQUID COMPOSITION, SOLID COMPOSITION, AND CARRIER CONCENTRATION OF BRIDGMAN-GROWN CRYSTALS OF $\text{Pb}_{1-x}\text{Sn}_x\text{Te}$			
Liquid Composition x	First-to-Freeze Solid Composition x	First-to-Freeze Hole- Carrier Concentration at 77°K (cm^{-3})	Hall Mobility at 77°K
0.0	0.0	3.0×10^{18}	—
0.2	0.127	3.1×10^{19}	940
0.3	0.20	2.4×10^{19}	240
0.7	0.62	3.0×10^{20}	60

2. Isothermal Annealing

It is well known that excess Pb and excess nonmetal defects introduce donor and acceptor levels, respectively, in the energy band structure of lead salts. The defect concentrations can be altered by a variety of annealing techniques. The isothermal annealing technique, which was first used by Brebrick on PbTe, has been used to obtain the solidus lines on the metal-rich side for various compositions in the $\text{Pb}_{1-x}\text{Sn}_x\text{Te}$ system. This technique involves the equilibration under isothermal conditions of a powder of known composition with a crystal of any initial defect concentration.

Bridgman-grown crystals of 1-mm thickness were sealed in evacuated quartz ampoules, and separated by a shelf from metal-rich powder (~5-percent metal-rich) of the same Pb/Sn ratio as the crystal. The crystals were annealed for various times and temperatures, and quenched in water. Resistivity, Hall coefficient, and Seebeck coefficient (α) measurements have been carried out on the crystals. Pertinent data obtained are presented in Table I-2.

By the incorporation of copper by diffusion, n-type material with a carrier concentration of $1.4 \times 10^{19}/\text{cm}^3$ was prepared for $x = 0.20$. The results of the isothermal annealing experiments on $\text{Pb}_{1-x}\text{Sn}_x\text{Te}$ are consistent with previous investigations^{28,29} in this area.

3. Vapor Growth

$\text{Pb}_{1-x}\text{Sn}_x\text{Te}$ crystals were vapor-grown at various temperatures between 700° and 825°C, using a 10-g powdered source ingot of various compositions, and air-cooled from the growth temperature. The source ingot was prepared from a 100-g mixture of the components which had been heated above the melting point and water-quenched.

For $0.16 \leq x \leq 0.20$, p-type crystals were grown using metal-saturated source powders. An n-type skin, which is believed to form due to the preferential loss of Te (and probably Sn)

TABLE I-2 RESULTS OF ISOTHERMAL ANNEALING EXPERIMENTS OBTAINED ON BRIDGMAN-GROWN CRYSTALS				
Composition $\text{Pb}_{0.8}\text{Sn}_{0.2}\text{Te}$				
Sample Temperature (°C)	Annealing Time (hr)	α , $\mu\text{V}/^\circ\text{K}$ at 300°K	Hole-Carrier Concentration at 77°K (cm^{-3})	Hall Mobility at 77°K ($\text{cm}^2/\text{V-sec}$)
825	23	93	1.2×10^{19}	2,100
750	100	167	3.7×10^{18}	6,900
700	314	235	1.8×10^{18}	12,000
650	293	221	2.8×10^{18}	9,000
Composition $\text{Pb}_{0.832}\text{Sn}_{0.168}\text{Te}$				
750	100	179	3.3×10^{18}	5,100
700	312	202	1.4×10^{18}	4,750
650	312	209	6.5×10^{17}	9,950
Composition $\text{Pb}_{0.87}\text{Sn}_{0.13}\text{Te}$				
700	312	235	2.7×10^{17}	20,000
650	312	245	2.2×10^{17}	18,700

from the surface during the cooling process, was observed on the crystals. For $x \leq 0.10$, only n-type crystals were grown from metal-saturated sources.

T. C. Harman
Mary C. Finn
A. E. Paladino

D. NEGATIVE RESISTIVITY EFFECTS IN CdTe

The following is the abstract of a thesis submitted to the Department of Electrical Engineering, M.I.T. on 19 January 1967 in partial fulfillment of the requirements for the degrees of Master of Science and Electrical Engineer.

"Observations of Gunn oscillation waveforms in n-CdTe are found to be consistent with the electric-field-controlled differential negative resistivity of the transferred-electron model. A threshold field of about 10,500 V/cm and a domain transit velocity of about 7×10^6 cm/s are determined.

"A current runaway process has been discovered which competes with the Gunn effect in CdTe. After several cycles of Gunn oscillations, the sample current rises while the sample voltage drops. During the runaway, band-gap radiation ($\sim 9000 \text{ \AA}$) is observed to be emitted in filaments reaching from one contact to the other. The effect is what one would expect if the material had a current-density-controlled differential negative resistivity. The conductivity increase is ascribed to excess hole-electron pairs rather than impact-ionization of impurities because the number of band-gap photons emitted from the sample after turn-off of the current pulse is at least ten percent of the number of excess electrons present during the pulse. Hole injection from contacts can be eliminated since short pulse (3 ns) experiments show light being emitted across the entire filament length. Low-field avalanche of the type proposed by Copeland³⁰ is suggested as the mechanism for the hole-electron pair generation and the accompanying negative resistivity."

M. R. Oliver

REFERENCES

1. C.E. Hurwitz, Appl. Phys. Letters 8, 121 (1966), DDC 642201.
2. H. Rodelt, Z. Naturforsch 15a, 269 (1960).
3. E.J. Sternglass, Phys. Rev. 95, 345 (1954).
4. J.E. Holliday and E.J. Sternglass, J. Appl. Phys. 28, 1189 (1957).
5. L. Holland, Vacuum Deposition of Thin Films (Wiley, New York, 1958), p.322.
6. P.J. Van Heerden, Phys. Rev. 106, 468 (1957).
7. K.A. Gale, Thesis, GNE/Phys/63-9, U.S. Air Force Institute of Technology, Wright-Patterson Air Force Base, Dayton, Ohio (1963).
8. W. Shockley, Solid-State Electron. 2, 35 (1961).
9. Yu. M. Popov, Soviet Researches on Luminescence, edited by D.V. Skobel'tsyn (Consultants Bureau, New York, 1964), p.62.
10. D.C. Reynolds, C.W. Litton, and T.C. Collins, Phys. Stat. Sol. 9, 645 (1965); 12, 3 (1965); and references cited therein.
11. E.T. Handleman and D.G. Thomas, J. Phys. Chem. Solids 26, 1261 (1965).
12. C.E. Hurwitz, IEEE J. Quant. Electron. QE-2, 17 (1966).
13. C. Benoit à la Guillaume and J.M. Debever, Compt. rend. 261, 5428 (1965); IEEE J. Quant. Electron. QE-2, 65 (1966).
14. D.C. Reynolds, private communication.
15. D.G. Thomas and J.J. Hopfield, Phys. Rev. 128, 2135 (1962).
16. R.H. Bube, Photoconductivity of Solids (Wiley, New York, 1960).
17. V.E. Kozhevnikov, Fiz. Tverd. Tela 8, 2478 (1966).
18. J.F. Dewald, J. Electrochem. Soc. 104, 244 (1957).
19. J.D. Venables and R.M. Broudy, J. Electrochem. Soc. 107, 296 (1960).
20. L.L. Chang and W.E. Howard, Appl. Phys. Letters 7, 210 (1965).
21. K.N. Moffitt and R.K. Mueller, J. Appl. Phys. 35, 1563 (1964).
22. R.K. Mueller and R.L. Jacobson, J. Appl. Phys. 35, 1521 (1964).
23. F.F. Sznosov, Izv. VUZ Fizika No. 4, 80 (1958).
24. G.K. Eaton, et al., J. Phys. Chem. Solids 23, 1473 (1962).
25. C.A. Mead and W.G. Spitzer, Phys. Rev. 134, A713 (1964).
26. G.W. Gobeli and F. G. Allen, Phys. Rev. 137, A245 (1965).
27. H.L. Henneke, J. Appl. Phys. 36, 2967 (1965).
28. N. Kh. Abrikosov, K.A. Dvuldina, and T.A. Danilyan, Zh. Neorgan. Khim. 3, No. 7, 1632 (1958).
29. A.A. Machonis and I.B. Cadoff, Trans. Met. Soc. AIME 230, 333 (1964).
30. J.A. Copeland, Appl. Phys. Letters 9, 140 (1966).

II. OPTICAL TECHNIQUES AND DEVICES

A. OBSERVATION OF THEORETICALLY PREDICTED 10.6- μ m HETERODYNE SENSITIVITY IN Ge:Cu

Recently, we reported^{1,2} on a measurement of the S/N ratio and minimum detectable power for heterodyne detection of scattered radiation at 10.6 μ m. Using photoconductive Ge:Cu as the detector, the observed minimum detectable power was found to be within 10 dB of the theoretical result for the perfect quantum counter, $h\nu\Delta f = 1.9 \times 10^{-20}$ W/Hz bandwidth.

In calculating the theoretically expected result for a real photoconductive detector, however, the presence of both generation-recombination noise and of a quantum efficiency η differing from unity tends to degrade the S/N ratio. Taking these effects into account, the minimum detectable power P_s^{\min} is given by $(2/\eta) h\nu\Delta f$ rather than by $h\nu\Delta f$ as in the ideal case.^{3,4} For the detector used in these experiments, $\eta \approx 0.5$, and the expected value of P_s^{\min} is therefore $4h\nu\Delta f \approx 7.6 \times 10^{-20}$ W/Hz beamwidth.

Using the same modified Michelson interferometer and experimental conditions as used previously,^{1,2} we have observed this theoretically predicted heterodyne sensitivity. The results of this measurement are shown in Fig. II-1. The solid line is the observed S/N power ratio $(S/N)_{\text{power}}$ of the heterodyne signal as a function of the signal beam radiation power P_s . With a heterodyne signal centered at about 70 kHz and an amplifier bandwidth of 270 kHz, the experimentally observed minimum detectable power P_s^{\min} is seen to be 2×10^{-14} W. In a 1-Hz bandwidth, this corresponds to a minimum detectable power of 7×10^{-20} W, which is to be compared with the expected value of $4h\nu\Delta f \approx 7.6 \times 10^{-20}$ W calculated above. It is therefore clear that the observed results are within 6 dB of the theoretically perfect quantum counter, and are in substantial agreement with the theoretical result expected for the Ge:Cu detector used in these experiments.

A sample waveform of the heterodyne signal voltage in the time domain (for a signal beam power of 1×10^{-8} W) is shown in Fig. II-2(a). The predominant frequency observed corresponds to a period of 14 μ sec. The power spectral density of the heterodyne signal (as a function of frequency) is shown in the typical trace of Fig. II-2(b). A Panoramic model SB-15a ultrasonic spectrum analyzer, operated with a trace sweep speed of $\approx 4 \text{ sec}^{-1}$, was used for the observations. The center frequency of 70 kHz is seen to correspond to the period of 14 μ sec observed in Fig. II-2(a). Both traces were obtained directly across the (1-kohm) photoconductor load resistor.

M. C. Teich
R. J. Keyes
R. H. Kingston

B. PHOTOVOLTAIC HETERODYNE DETECTION OF CO₂ LASER RADIATION IN Pb_xSn_{1-x}Te

Heterodyne detection has been performed at 10.6 μ m in a Pb_{0.83}Sn_{0.17}Te diode⁵ operated in the photovoltaic mode. The experimental arrangement is shown in Fig. II-3. This setup is similar to that used in experiments with photoconductive Ge:Cu (Refs. 1 and 2). Here, however,

Section II

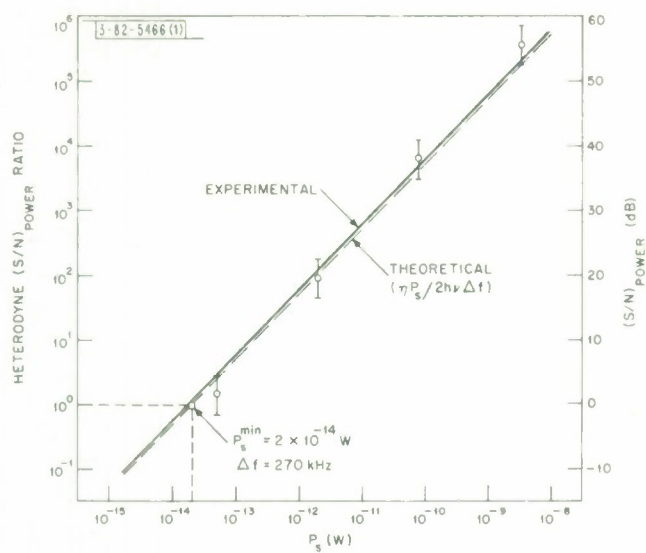


Fig. 11-1. Heterodyne S/N ratio vs signal power for Ge:Cu detector.

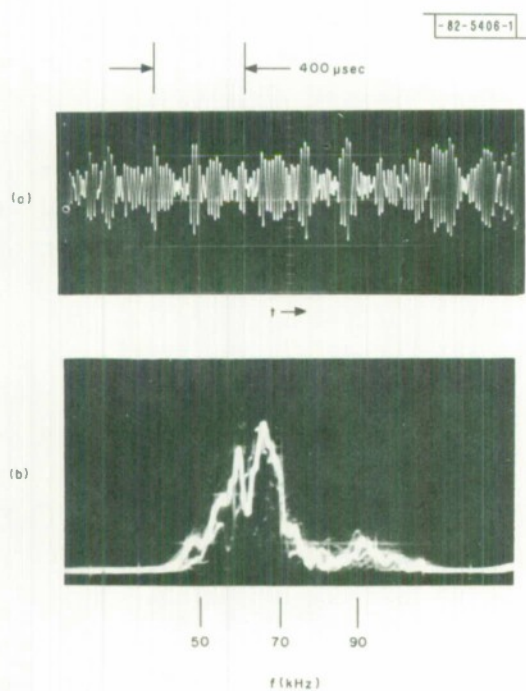


Fig. 11-2. (a) Sample waveform of heterodyne signal; (b) power-spectral density of heterodyne signal.

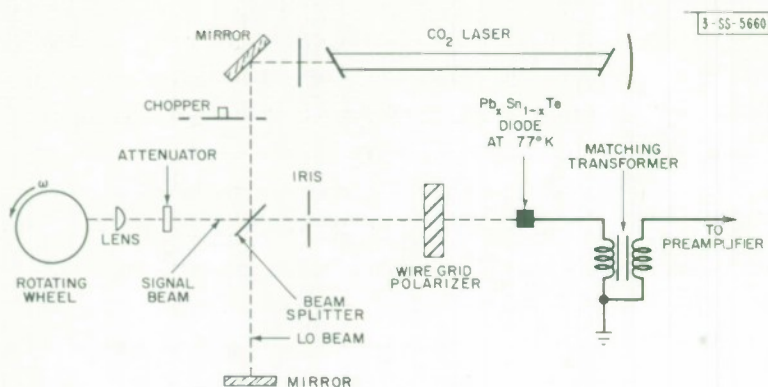


Fig. II-3. Experimental arrangement for heterodyne detection at $10.6\ \mu\text{m}$ in photovoltaic $\text{Pb}_x\text{Sn}_{1-x}\text{Te}$.

the device is operated as a low-impedance photovoltaic detector at liquid nitrogen temperatures (77°K), rather than as a photoconductor at liquid helium temperatures (4°K). The experimental procedure is similar to that described in experiments with $\text{Ge}:\text{Cu}$.

The detector output voltage has been observed to be proportional to the square root of the signal beam power ($\propto \sqrt{P_s}$), as would be expected for heterodyne operation. However, the S/N ratio is higher than the theoretically calculated result, and attention is presently being directed to improve this aspect of the experimental operation.

M. C. Teich

C. STABILITY MEASUREMENTS OF $\text{CO}_2\text{-N}_2\text{-He}$ LASERS AT $10.6\text{-}\mu\text{m}$ WAVELENGTH

The short-term stability⁶ of the beat frequency⁷⁻⁹ of two stable, single-frequency (TEM_{00q} mode) $\text{CO}_2\text{-N}_2\text{-He}$ lasers has been measured. Both lasers were sealed-off and free-running without any feedback stabilization. The width of the spurious frequency modulation was typically of the order of 9 and 20 kHz for observation times of 3×10^{-2} and 1 sec, respectively. On one occasion, the frequency spread remained less than the spectrum analyzer resolution ($\sim 500\text{ Hz}$) for several seconds, and the slow drift did not exceed a few kilohertz for several minutes. The observed frequency jitter was caused by environmental fluctuations such as acoustic vibrations, plasma instabilities, power supply noise, variations of temperature and pressure, etc. Therefore, these measurements should not be confused with the ultimate spectral width of a laser oscillator; this linewidth is dominated by frequency fluctuations caused by the random walk of the oscillation phase under the influence of spontaneous emission or quantum noise.⁸ For a two-level system, the linewidth of the laser above the threshold of oscillation is approximately¹⁰⁻¹³

$$\Delta f \sim \frac{\pi h f}{P} (\Delta f_{\text{cavity}})^2 \quad (1)$$

where Δf is the full width between the half-power points of the Lorentzian line, h is Planck's constant, f is the frequency, P is the power output of the laser, and Δf_{cavity} is the "cold" bandwidth of the laser cavity. Even though the $\text{CO}_2\text{-N}_2\text{-He}$ laser is not a relatively simple two-level system, Eq. (1) was used to estimate the linewidth for a power output of $P = 10^{-1}\text{ W}$ and a full cavity bandwidth of $\Delta f_{\text{cavity}} \approx 6\text{ MHz}$. These parameters were typical of the experiments described here, and the resulting linewidth estimate was $\Delta f \sim 2 \times 10^{-5}\text{ Hz}$.

Section II

The lasers used in these experiments were DC-excited internal mirror tubes, in which the mirror holders were rigidly held apart by four invar rods. In most mechanical detail, these lasers are similar to those employed in earlier intensity fluctuation experiments¹⁴ using HeNe lasers operated at 6328 Å. Modifications included a water-cooled discharge tube section operable with either a 10- or 20-cm length gas discharge in the optical cavity. In addition, a differential screw tuning mechanism was added to one of the mirror holders to permit a 3.5-μm-per-turn axial motion of the laser mirror. In the design of this device, utmost care was taken to insure both rigidity and pure axial motion. The tuner was inside the tube envelope and could be completely decoupled from the actuator that moved it from the outside.

A nearly semiconfocal optical cavity configuration was used in both lasers. The distance between the totally reflecting 1-m radius mirror and the 2-percent transmission flat multiple dielectric layer coated mirror was 48.5 cm. A 5.6-mm beam-limiting aperture was placed in front of the spherical mirror, resulting in about a 10:1 relative diffraction loss ratio between the lowest loss off-axis (TEM_{10q}) mode and the desired fundamental (TEM_{00q}) mode.¹⁵ The overall gain of the lasers was adjusted so that only fundamental (TEM_{00q}) mode operation could overcome the combination of mirror and diffraction losses.

During the stability measurements, the lasers were acoustically isolated by a wooden box lined with fiberglass. This box was supported by a heavy granite slab which was, in turn, isolated from floor vibrations by inflated rubber inner tubes. After careful alignment, the two laser beams were recombined by a dielectrically coated Irtan beam-splitter. The recombined beam was detected by a liquid nitrogen cooled gold-doped germanium detector which was externally loaded by 1 kohm. The RC time constant of the detector, together with the Tektronix 1121 amplifier following it, limited the observation of beat frequencies to less than 30 MHz. The low frequency limit was set by the width of the zero-spike on the spectrum analyzer and by frequency jitter.

Both lasers were sealed off with the following gas fill: $CO_2 \sim 3$ torrs; $N_2 \sim 3$ torrs; He ~ 12 torrs. The final seal-off pressures were chosen in part as a result of detailed measurements of power and discharge characteristics as functions of gas mixtures and current, and in part as a result of life-test data by Carbone.¹⁶ The lasers have been sealed off for about 7 weeks, and have operated for approximately 100 to 200 hours. At the time of this writing, both lasers were still in operating condition.

All the aforementioned design considerations were experimentally verified. Not only was the familiar circular spot pattern characteristic of the TEM_{00q} modes observed, but a single beat-frequency was always observed on the oscilloscope and on the spectrum analyzer. Figures II-4(a) and (b) show a 7.5-MHz beat-frequency on a Tektronix 585 scope and on a Hewlett-Packard 851 spectrum analyzer, respectively. Note that both instruments were operated in the internal trigger mode (not single scan) so that the film exposure times used allowed the integration of many traces on both the scope and spectrum analyzer photographs. The largest spike in the center of Fig. II-4(b) is the zero center frequency and is entirely instrumental. The two other symmetrical spikes at 7.5 MHz to either side of zero correspond to the 7.5-MHz sine wave. Also, it should be noted that the spectrum analyzer display was logarithmic and no other beat-frequency could be observed within the 60-dB dynamic range of this instrument.

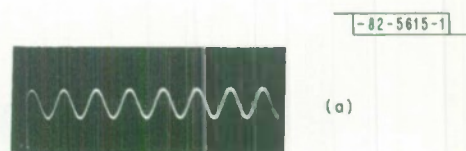
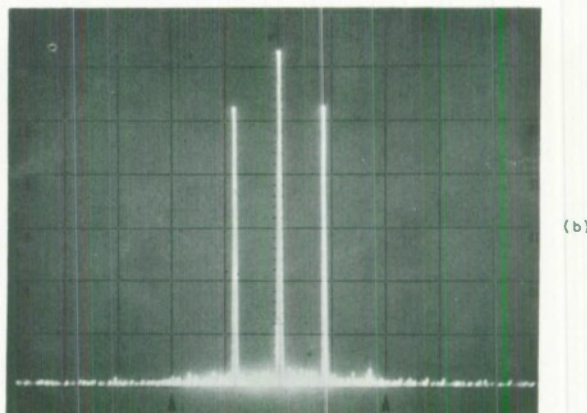


Fig. II-4. Beat-frequency of two lasers at 7.5 MHz.
 (a) Oscilloscope trace: 10^{-7} -sec/cm horizontal sweep, internal trigger operation, 0.5-sec exposure time.
 (b) Spectrum analyzer display: vertical scale logarithmic, zero center frequency, 10-MHz/cm horizontal dispersion, 3×10^{-3} -sec/cm sweep rate, 10-kHz IF bandwidth, internal trigger operation, 0.2-sec exposure time.



By using the tuning mechanism previously described, the observed beat-frequency could be tuned from tens of kHz to 28 MHz, and displays similar to those of Fig. II-4 were produced. Figure II-5(a) shows a typical spectrum analyzer photograph of a 7.5-MHz beat-frequency similar to that of Fig. II-4. However, the frequency dispersion has been narrowed to 30 kHz/cm and to the IF bandwidth of 1 kHz. The combination of a 1-sec exposure time and the 3×10^{-3} -sec/cm sweep rate of Fig. II-5(a) allowed the integration of approximately 33 consecutive traces on the photograph. Thus, Fig. II-5(a) indicates an approximately 20-kHz wide envelope for the combined frequency drift and jitter contributed by both lasers. For an exposure time of 3×10^{-2} sec, an approximately 9-kHz envelope width was typical. Single-scan pictures at 3×10^{-3} -sec/cm sweep rates seldom yielded anything different from the frequency spike caused by a Hewlett-Packard 608 generator which is shown in Fig. II-5(b). At this point, it should be emphasized that the effective resolution of a spectrum analyzer is not necessarily given by the IF bandwidth B , but rather by the combination of B (in hertz), sweptime T (in seconds), and dispersion Δf (in hertz). For most conventional spectrum analyzers with a Gaussian IF response, the effective resolution R may be shown to be

$$R = B \left[1 + 0.195 \left(\frac{\Delta f}{TB^2} \right)^2 \right]^{1/2} \quad (2)$$

Thus, in spite of a 1-kHz IF bandwidth, the effective resolution was approximately 4.5 kHz for Figs. II-5(a) and (b), both of which were photographed with identical analyzer and camera settings.

The stability thus far observed is considered poor because of relatively bad environmental conditions. On one occasion at least, the beat-frequency fluctuation stayed well within the

Section II

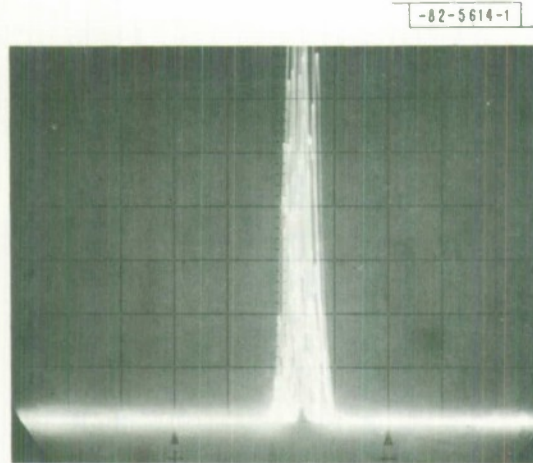


Fig.II-5(a). Beat-frequency of two lasers at 7.5 MHz on a higher resolution spectrum analyzer display: vertical scale linear, 30-kHz/cm horizontal dispersion, 3×10^{-3} -sec/cm sweep rate, 1-kHz IF bandwidth, internal trigger operation, 1-sec exposure time.

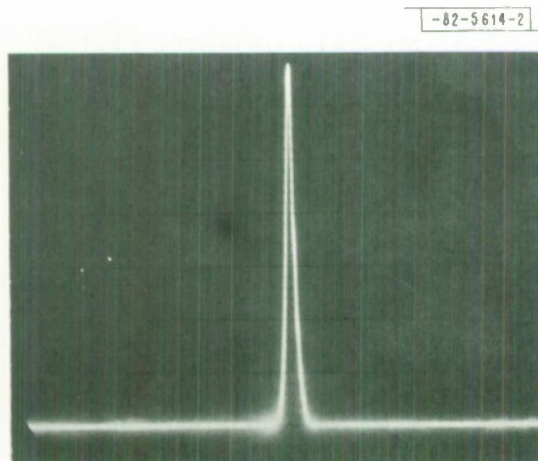


Fig.II-5(b). Output of Hewlett-Packard 608 signal generator; spectrum analyzer settings and exposure time are identical to those of Fig.II-7(a).

approximately 500-Hz resolution limit of a Panoramic spectrum analyzer for several seconds, and the slow drift did not exceed a few kilohertz on a 1-kHz/cm display for several minutes. This observation shows that the conservative but more typical stability figures given above can be improved with proper care and equipment.

The measurements described here are considered only preliminary in order to test some of the design features of the lasers and to facilitate the choice among the different approaches pertaining to more refined frequency stability measurements as partially outlined by Siegman, *et al.*,⁸ and in Ref. 6. We hope that future experiments with improved lasers and experimental setup will result in better stability figures.

C. Freed

D. CO₂ 10.6- μ LASER

The CO₂ laser tube discussed in the last Solid State Research Report^{*} was operated for several 100-hour periods, each with a new pressure fill of 2 torrs CO₂, 2 torrs N₂, and 7 torrs He. The time periods were not continuous, but accumulated over approximately a 1000-hour interval so that several different ballast volumes could be used and gas samples mass spectrum analyzed after different time intervals of operation.

Gas samples were mass spectrum analyzed by the Rare Gas Department of Air Reduction Company, Inc., and the results of one sample taken from a tube after 20 hours of operation are presented in Table II-1.

TABLE II-1 MASS SPECTRUM ANALYSIS OF GAS SAMPLE FROM CO ₂ LASER		
Constituent	Percent of Constituent by Pressure	Percent of Original Constituent by Pressure
H ₂	0.2	—
He	60.88	63.64
N ₂	18.0	18.18
CO ₂	9.66	18.18
O ₂	3.43	—
CO	8	—
C ₂ N ₂	<15 ppm [†]	—
NO } N ₂ O } NO ₂ }	<100 ppm	—
† Parts per million.		

* Solid State Research Report, Lincoln Laboratory, M.I.T. (1966:4), p. 17, DDC 647688.

Section II

Analyses of other samples show similar results with a large relative percentage of CO compared with percentages of CO_2 and N_2 , and this held even in an analysis taken after 95 hours of operation. Because of the CO formation, the CO_2 pressure is overfilled relative to the N_2 pressure. The data show that the CO density may saturate at approximately 8 percent of the tube pressure or possibly slowly decrease from this value in the time period of 100 hours. If these results are indicative of future findings, then the major chemistry in the CO_2 laser discharge is the formation of CO and O_2 from CO_2 up to a given density of CO. The saturation of CO may be explained by the large He density which acts as a third body in the reaction



which becomes an appreciable process when CO reaches a given density. Other molecules (especially N_2O), if formed, are done so in a reversible reaction, which maintains a low density, so that the N_2 content is changed very little during the tube operating interval. The high relative percentage of CO and O_2 formed in the discharge can explain the lower power efficiency per unit volume¹⁷ of a sealed-off tube compared to a tube that has gas rapidly flowing through the laser. Instead of an optimum tri-gas mix of N_2 , CO_2 , and He, a mix of five gases (N_2 , CO_2 , He, CO, and O_2) is present, which unfortunately has a lower power efficiency because CO is less efficient than N_2 in its role of exciting the upper CO_2 laser level.

Figure II-6 shows the output power as a function of operating time. Three curves are shown, each with a different ballast volume. Indications are that the ballast has some effect on tube life,

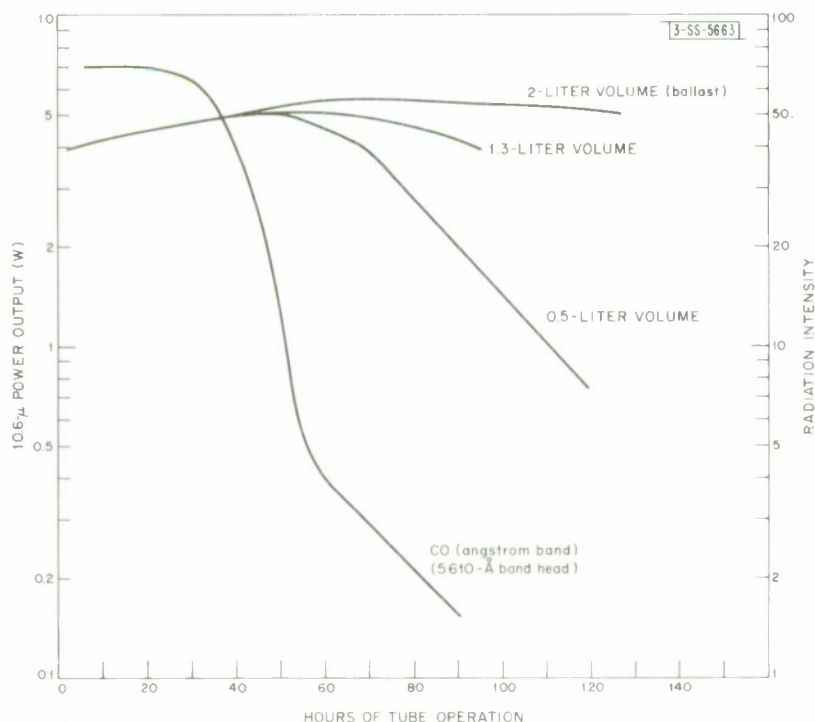


Fig. II-6. CO_2 laser output power and spontaneous radiation emission as function of operating time.

i.e., a larger volume means a longer life, but the reasons for this are not yet completely clear. In Fig. II-6, the CO band head (5610 \AA) shows a functional decrease in intensity that follows a simultaneously measured power decrease as observed for the 0.5-liter ballast curve, but the CO density within the fill should not be changing an appreciable amount. Therefore, to drastically change the measured power and radiation output, other undesirable processes (such as a slow increase in impurities from the tube electrodes and walls, and/or a minute atmospheric leak) must become important as the laser operates. There is some experimental evidence to support the existence of these processes, but results are to be rechecked. In either case, the ballast volume will put off the appearance of deleterious effects.

Work is continuing to confirm the above results and to strive for a sealed-off CO₂ laser with a lower CO and O₂ content by trying to maintain a mix similar to that in a flowing gas tube.

R. J. Carbone

REFERENCES

1. M. C. Teich, R. J. Keyes, and R. H. Kingston, *Appl. Phys. Letters* 9, 357 (1966).
2. Solid State Research Report, Lincoln Laboratory, M.I.T. (1966:4), p. 15, DDC 647688.
3. S. Jacobs and P. Rabinowitz, "Optical Heterodyning with a CW Gaseous Laser," in *Quantum Electronics III*, edited by P. Grivet and N. Bloembergen (Columbia University Press, New York, 1964), p. 481.
4. R. C. Jones, *Proc. IRE* 47, 1481 (1959); A. van der Ziel, *Fluctuation Phenomena in Semi-Conductors* (Academic Press, New York, 1959), pp. 22 and 65.
5. I. Melngailis and A. R. Calawa, *Appl. Phys. Letters* 9, 304 (1966).
6. *Proc. IEEE* 54 (February 1966), Special Issue on Frequency Stability.
7. T. S. Jaseja, A. Javan, and C. H. Townes, *Phys. Rev. Letters* 10, 165 (1963).
8. A. E. Siegman, B. Daino, and K. R. Manes, "Preliminary Measurements of Laser Short-Term Frequency Fluctuations," to be published in the *IEEE J. Quant. Electron.* (May 1967).
9. R. A. Brandewie, W. T. Haswell, III, and R. H. Harada, *IEEE J. Quant. Electron.* QE-2, 756 (1966).
10. M. Scully and W. E. Lamb, Jr., "Quantum Theory of an Optical Maser," submitted to *Phys. Rev. Letters*.
11. H. J. Pauwels, *IEEE J. Quant. Electron.* QE-2, 54 (1966).
12. M. Lax, *Physics of Quantum Electronics, Conference Proceedings*, edited by P. L. Kelley, B. Lax, and P. E. Tannenwald (McGraw-Hill, New York, 1966), p. 735.
13. V. Korenman, *ibid.*, p. 748.
14. C. Freed and H. A. Haus, *Phys. Rev.* 141, 287 (1966), DDC 633186.
15. T. Li, *Bell System Tech. J.* 44, 917 (1965).
16. R. Carbone, private communication.
17. G. J. Schulz, *Phys. Rev.* 135, A988 (1964).

III. MATERIALS RESEARCH

A. ARC-MELTING FURNACE FOR CZOCHRALSKI GROWTH OF SINGLE CRYSTALS

In order to grow single crystals from the melt at high temperatures, it is necessary both to supply enough heat for melting the material and to contain the liquid produced. In the Verneuil method, no crucible is required since a very small quantity of melt produced by a flame, arc, or plasma is retained in the form of a molten cap on the source rod by means of surface tension. The Czochralski method is capable of producing better crystals because it uses a large melt which contributes to interface stability and also acts as a reservoir into which impurities can be rejected. However, this method generally has required a crucible, and it is often difficult to find a crucible material that does not contaminate the melt. To solve this problem, an arc-melting furnace has been developed which permits Czochralski growth without a hot crucible.

In conventional arc melting, an arc is struck in argon between a tungsten electrode and the sample, which rests on a water-cooled copper hearth. Because of the poor thermal contact between the sample and the hearth, the sample can be almost entirely molten while the hearth remains at a relatively low temperature. A hot crucible is not required, since the melt is supported by a solid shell of the same substance in contact with the hearth. This method has been used to prepare polycrystalline "buttons" of a wide variety of metals, semiconductors, and insulators with melting points from as low as 200°C to as high as 3600°C. There is no appreciable contamination by either the electrode or the hearth, since the concentration of either tungsten or copper in such buttons rarely exceeds a few parts per million.

The arc-melting furnace constructed for Czochralski growth is shown in Fig. III-1. It uses three cathodes to heat the periphery of the melt, which is supported by a water-cooled copper crucible. The furnace consists of an upper cathode member and a lower anode member, which are insulated from each other by a pyrex ring. The upper member contains a central hole through which a water-cooled seed rod, mounted in a ball and socket, is raised or lowered by a pulling mechanism. There are also six holes equally spaced around the circumference: three containing tungsten electrodes mounted in ball and O-ring sockets, and three sealed with quartz windows. The lower member consists of a central graphite or copper piston (2.5 cm in diameter) which can be raised or lowered manually inside a copper cylinder, which is taper-fitted into a water-cooled brass cylinder containing the gas ports and current leads. The furnace is powered by a 500-A DC welding generator, and each arc is stabilized by a variable ballast resistor.

The furnace is loaded by placing a 10- to 20-g charge of source material in the crucible formed by lowering the central piston below the top of the copper cylinder. The system is then flushed with argon. A flow rate of 4 l/min. is satisfactory, since the total gas volume is only about 200 cm³. Arcs are struck from the three electrodes to the walls of the copper cylinder, and the piston is raised until the arcs strike the charge and a melt is formed. Since the arcs strike the melt tangentially, a stirring action is produced in the liquid. (For compounds which can be prepared by arc melting, it is frequently convenient to charge the furnace with the appropriate constituents and perform the synthesis just before crystal growth. This procedure

Section III



Fig. III-1. Arc-melting furnace for Czochralski growth of single crystals.



Fig. III-2. Crystal of NbO being grown in arc-melting furnace.

has been used in the growth of TiO , Ti_2O_3 , and NbO , which are prepared from a charge consisting of the metal and its highest oxide.)

To initiate crystal growth, the seed rod (usually tungsten) is dipped into the melt and the power is adjusted to produce a growth interface a few millimeters in diameter. The rod is gradually raised until ~ 5 mm of growth has occurred, after which the interface is moved to another part of the melt by shifting the rod. Following ~ 5 mm of additional growth, the interface is moved to the center of the melt. These operations form a V-shaped section in the boule which helps to reduce the degree of polycrystallinity. Finally, the power is reduced to increase the diameter of the crystal to the desired size, and growth is continued at a rate which is typically several inches per hour. A crystal of NbO growing under these conditions is shown in Fig. III-2.

A large number of NbO_x boules, with $0.95 < x < 1.02$, have been grown in the arc-melting furnace from melts with $0.94 < x < 1.07$. Some of these boules are single crystals, and all contain grains large enough for electrical measurements. The furnace has also been used to grow a number of Ti_2O_3 crystals containing various dopants. The versatility of the apparatus is illustrated by Fig. III-3, which shows boules of seven different materials all grown in a single day. Although some of the boules are polycrystalline, it is likely that single crystals could be obtained by using higher quality source material and a seed more suitable than tungsten. Successful growth of Sn and Ge, the lowest melting materials, required low currents (about 10 A per arc), large quantities of melt, and good wetting of the seed rod in order to maintain a sufficient temperature gradient. The boules of V, Cr, VO, and Ti_2O_3 were grown easily with currents between 40 and 60 A per arc. Difficulties encountered in growing the highest melting material, Nb, showed that growth at temperatures above 2500°C would require currents higher than the maximum of 60 A per arc presently available.

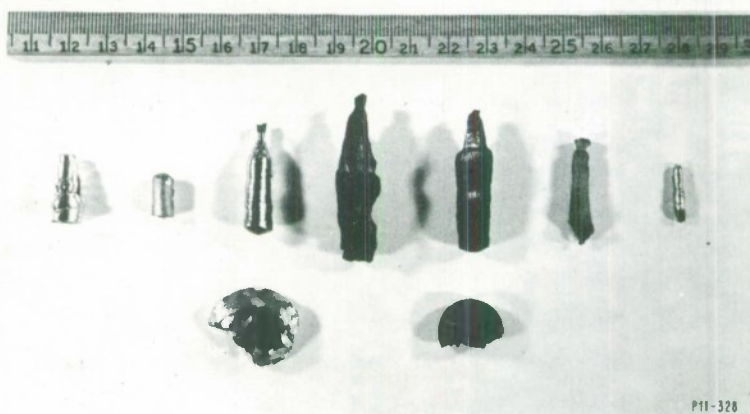


Fig. III-3. Boules grown in arc-melting furnace. Left to right, in order of increasing melting point: Sn, Ge, V, VO, Ti_2O_3 , Cr, and Nb.

Section III

All the crystals grown so far in the arc-melting furnace are good conductors, since the present method relies on the excellent heat transfer from an arc to a conductor. In order to obtain nonconducting crystals, some change in melting technique¹ would be required. The present apparatus could be used without modification with nitrogen or hydrogen atmospheres, but special cathodes² would be necessary for growth in oxygen.

T. B. Reed
E. R. Pollard

B. GROWTH OF MnI_2 SINGLE CRYSTALS

Single crystals of MnI_2 , a compound with the CdI_2 layer structure, have been prepared by condensation from the vapor phase and by freezing from the melt. The crystals were grown in a 30-mm-diameter quartz tube which was placed in a resistance-heated muffle furnace. The tube was loaded with a charge of iodine crystals near the inlet end and a charge of manganese metal further inside. Helium gas at one atmosphere pressure was passed through the tube.

During crystal growth, the temperature along the tube increased from room temperature at the inlet to a maximum of 760°C , decreased to 720°C near the center of the furnace, increased again to 760°C , and then decreased to room temperature at the outlet. The temperatures of the iodine and manganese charges were about 70° and 720°C , respectively. Under these conditions, iodine vapor transported by the helium reacted with the manganese to produce MnI_2 vapor. Part of the latter condensed in the minimum temperature region at the center of the tube to form a pool of liquid; the remainder was transported to the cooler parts of the tube, where it condensed as pink platelet crystals. When the furnace was turned off, red grains of MnI_2 as large as 1 cm on an edge and several millimeters thick were formed by solidification of the melt. Since MnI_2 is very hygroscopic, the crystals deteriorate quite rapidly if exposed to air.

T. B. Reed
W. J. LaFleur

C. HIGH-PRESSURE PHASE DIAGRAM OF InSb

The existence of the high-pressure InSb phase designated as InSb-III was reported previously.³ The superconducting transition temperature T_c for this phase was found to be $4.05 \pm 0.1^\circ\text{K}$, compared with $2.0 \pm 0.1^\circ\text{K}$ for the tetragonal InSb-II phase and $3.5 \pm 0.1^\circ\text{K}$ for the orthorhombic phase. With increasing temperature, InSb-II is transformed into InSb-III at $308 \pm 7^\circ\text{C}$ for a pressure of 37 kbars, and at $287 \pm 12^\circ\text{C}$ for 52 kbars.

In order to obtain additional information on the range of stability for InSb-III, T_c and x-ray diffraction measurements have been made on InSb samples annealed at 65 kbars for 1 to 15 days at temperatures between 100° and 400°C . The results are summarized in Table III-1. Only InSb-III and orthorhombic phases are present in any of the samples. The absence of InSb-II is consistent with the data of McWhan and Marezio,⁴ who report that at room temperature the orthorhombic phase is stable at 60 kbars.

The results listed in Table III-1 for samples annealed at 175° or below are inconsistent, since samples which were melted at 65 kbars before annealing have T_c values characteristic of InSb-III, while those which were not melted have T_c values of the orthorhombic phase. Although the data are not conclusive, we believe that the samples which were not melted had attained

TABLE III-1
DATA ON InSb SAMPLES ANNEALED AT 65 kbars

TABLE III-1				
DATA ON InSb SAMPLES ANNEALED AT 65 kbars				
Pretreatment	Annealing		T_c (°K)	Phase (x-ray)
	Temperature (°C)	Time (days)		
Equilibrium Samples				
Melted	400	1	3.97	—
Nane	250	4	3.87	—
Nane	225	10	3.85	III
Melted	225	4	3.89	III
Melted	200	15	3.88	—
Nane	175	11	3.45	Orthorhombic
Nane	150	4	3.39	Orthorhombic
Nane	100	7	3.55	—
Nonequilibrium Samples				
Nane	175	4	3.71	—
Melted	150	2	3.98	—
Melted	125	4	4.02	—
Melted	100	4	4.01	Contains III

thermal equilibrium during annealing, and that the orthorhombic phase is stable at these temperatures. The other samples crystallized from the melt in the InSb-III structure, since this phase is in equilibrium with the liquid at 65 kbars, and apparently were not annealed long enough to be transformed into the orthorhombic phase. Therefore, they are listed as nonequilibrium samples in Table III-1.

The data show clearly that InSb-III is the stable phase at 225°C, since it was observed for both samples annealed at this temperature, one of which had been melted and the other had not. Therefore, at 65 kbars the transition from the orthorhombic to InSb-III phase occurs close to 200°C.

A tentative pressure-vs-temperature diagram for InSb, based on all the data currently available, is shown in Fig. III-4. The dotted lines are schematic. The boundaries between InSb-III and the other solid phases between 65 and 80 kbars are drawn to indicate the influence of the triple point between InSb-II, InSb-III, and the orthorhombic phases. No precise data are available on the boundary between the InSb-II and orthorhombic phases. The resistivities of these phases are apparently too similar for the boundary to be determined by electrical measurements.

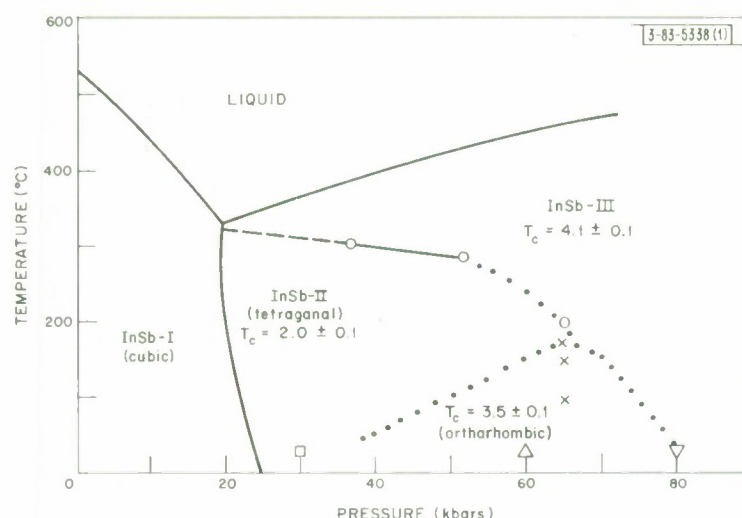


Fig. III-4. Pressure-vs-temperature diagram for InSb. Dashed extrapolation of boundary between InSb-II and InSb-III is consistent with thermodynamic data.⁸ Dotted lines are schematic. Observations of orthorhombic phase are indicated by: X (this work), Δ (McWhan and Marezio⁴), and \square (Kasper and Brondhorst⁷). The ∇ represents transition observed by Minamuro, *et al.*,⁵ to phase with $T_c = 4.8^\circ\text{K}$.

The transition from the orthorhombic to InSb-III phase at room temperature is shown at 80 kbars, where Minomura, *et al.*,⁵ observed a small peak in the resistance-vs-pressure curve. However, the phase which these authors obtained above 80 kbars may not be InSb-III, since they report a T_c value of 4.8°K .

On the basis of discontinuities in resistance-vs-temperature and resistance-vs-pressure curves, Kato and Ikezu⁶ have recently reported a phase boundary between 30 and 50 kbars which is similar in slope to the boundary between InSb-II and InSb-III shown in Fig. III-4, but which occurs at lower temperatures. We suggest that errors in their temperature values, which could have resulted because of high temperature gradients in their apparatus, probably account for the discrepancy between their results and the present ones.

M. D. Banus
Mary C. Lavine

D. BAND INVERSION IN $\text{Pb}_{1-x}\text{Sn}_x\text{Se}$ ALLOYS

Single crystal films of $\text{Pb}_{1-x}\text{Sn}_x\text{Se}$ alloys with rocksalt structure ($0 \leq x \leq 0.33$) have been deposited on freshly cleaved (100) faces of KCl substrates by means of an evaporation technique generally similar to those used to obtain single crystals of PbS, PbSe, and PbTe (Ref. 9) and of $\text{Pb}_{1-x}\text{Sn}_x\text{Te}$ alloys (Ref. 10). Determinations of composition by electron microprobe analysis show that most of the films are uniform in x , the mole-fraction of SnSe, to within the experimental accuracy of the microprobe, which is estimated to be ± 3 percent of x .

Measurements of resistivity and Hall coefficient (R_H) were made at 300° and 77°K by conventional DC potentiometric techniques. At 77°K , all the films measured have positive values of R_H , with hole concentrations ($p = 1/R_H e$) between 8×10^{16} and $3 \times 10^{18} \text{ cm}^{-3}$. By analogy

with PbSe, the acceptors are probably lattice defects (specifically, Pb and Sn vacancies) resulting from the presence of Se in excess of the stoichiometric composition. There appears to be no essential connection between net acceptor concentration ($N_A - N_D \approx p_{77}$) and Sn content.

Infrared transmission measurements between 2 and 25 μm were made on selected films at 300°, 195°, and 77°K. In order to evaluate the energy gap E_g in a consistent manner from the position of the absorption edge, E_g was taken to be the energy corresponding to the wavelength at which the absorption coefficient was $1.5 \times 10^3 \text{ cm}^{-1}$.

The variation of E_g with Sn content is shown in Fig. III-5. Dotted lines have been drawn at +0.05 and -0.05 eV to indicate that no values of E_g could be obtained between these limits, since transmission measurements were not made beyond 25 μm . (The significance of the negative sign adopted for certain values of E_g is discussed below.) The present values are seen to be in good agreement with values of E_g at 77°K corresponding to the emission wavelengths of diode lasers prepared from PbSe (Ref. 11) and $\text{Pb}_{0.96}\text{Sn}_{0.04}\text{Se}$ (Ref. 12). Films with sufficiently low Sn content exhibit the positive temperature coefficient of E_g which is characteristic of PbSe, PbTe, and PbS.

As shown in Fig. III-5, E_g for the $\text{Pb}_{1-x}\text{Sn}_x\text{Se}$ alloys initially decreases as x increases. At each of the temperatures investigated, E_g becomes so small with increasing x that the absorption edge shifts beyond 25 μm . However, when x exceeds 0.2, the absorption edge at 77°K once more becomes measurable and moves to shorter wavelengths. In this region of composition and temperature, therefore, E_g increases as x increases. The data also show that in this region (where E_g is assigned negative values in Fig. III-5) E_g decreases with increasing temperature, since E_g at 195°K is too small to be measured for any value of x above 0.15. Thus, for samples with sufficiently high values of x , both the composition and temperature dependence of E_g at low temperatures are opposite in sign to those for PbSe. This sign reversal shows that the $\text{Pb}_{1-x}\text{Sn}_x\text{Se}$ alloys exhibit the inversion of conduction and valence bands proposed¹³ for $\text{Pb}_{1-x}\text{Sn}_x\text{Te}$ alloys.

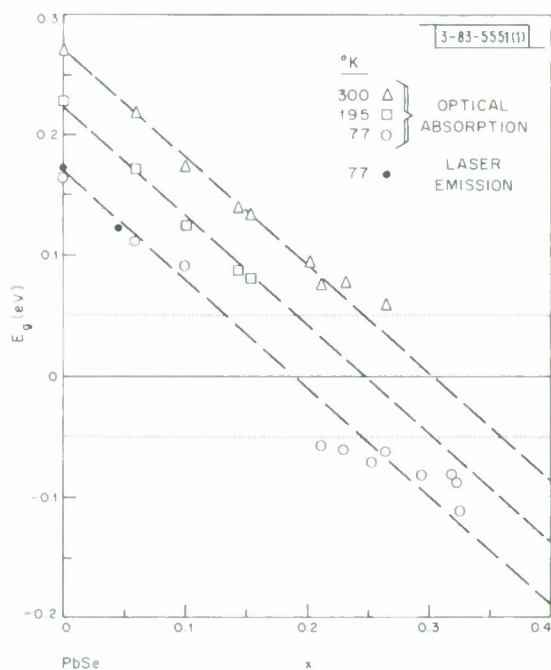


Fig. III-5. Variation of energy gap E_g with composition and temperature for $\text{Pb}_{1-x}\text{Sn}_x\text{Se}$ alloys with rocksalt structure. Dotted lines drawn at +0.05 and -0.05 eV indicate that no values of E_g could be obtained between these limits.

Section III

According to the band inversion model, as represented schematically in Fig. 2 of Ref. 13, the conduction and valence band extrema of PbTe are L_6^- and L_6^+ states, respectively. With increasing Sn content, these states approach each other, become degenerate at a value of x which increases with increasing temperature, and then interchange. Beyond the inversion point, where $E_g = 0$, the L_6^+ state forms the conduction band edge, and the L_6^- state forms the valence band edge. This band model should be directly applicable to the $Pb_{1-x}Sn_xSe$ alloys with rock-salt structure, since PbSe has essentially the same band structure as PbTe.

For the $Pb_{1-x}Sn_xTe$ alloys, the change in band structure with composition has been attributed to the influence of relativistic effects on the energies of the conduction and valence bands.¹³ It is probable that the changes in $Pb_{1-x}Sn_xSe$ band structure are also due principally to the difference between the relativistic energy shifts of the Pb and Sn atomic valence states.

In Fig. III-5, negative values of E_g have been assigned to those sample compositions and temperatures for which the energy bands are inverted from those in PbSe. Adopting this convention makes it possible to represent the data by straight lines, satisfying the equation E_g (eV) = $0.13 + (4.5 \times 10^{-4})T - 0.89x$. According to this equation, band inversion occurs at 77°, 195°, and 300°K for $x = 0.19$, 0.25, and 0.30, respectively.

A. J. Strauss

E. MAGNETIC PROPERTIES AND CRYSTAL STRUCTURE OF $MnYb_2S_4$

Magnetic interactions between rare-earth and 3d transition cations in crystals have not been extensively investigated. In an attempt to obtain additional information concerning such interactions, a magnetic and structural study has been made of the thio-spinel $MnYb_2S_4$. Spinel compounds (AB_2X_4), in which the A and B cations are situated in a highly covalent anion lattice, provide a favorable environment for interactions between magnetic cations. A variety of magnetic interactions have been observed in these compounds, but no magnetic study has been made on a spinel containing both rare-earth and transition cations.

$MnYb_2S_4$ can be prepared by passing H_2S over a stoichiometric mixture of the oxides.¹⁴ We have found it more satisfactory to synthesize the compound by reacting a stoichiometric mixture of Yb_2S_3 , manganese metal, and sulfur in an alundum crucible sealed in silica under vacuum and fired at 1300°C for 24 hours. The material obtained is microcrystalline and olive green in color.

The magnetic susceptibility of $MnYb_2S_4$ was measured as a function of temperature with a vibrating sample magnetometer. A plot of $1/\chi$ vs T for the data is shown in Fig. III-6. In the paramagnetic region, this plot has an inverse slope of 9.52, which is just equal to the sum of contributions from Yb^{3+} and high-spin Mn^{2+} , for which $\mu_{Mn} = 5.92\beta$. The magnetization depends linearly on magnetic field at both liquid nitrogen and liquid helium temperatures, which indicates that there is no magnetic interaction between the Yb^{3+} and Mn^{2+} ions down to low temperatures. The deviation from a straight line in the plot of Fig. III-6 at temperatures below 60°K can be attributed to the Yb^{3+} ions, since it is essentially the same as the deviation observed for YbF_3 (Ref. 15).

In order to refine the structure of $MnYb_2S_4$, the intensities of x-ray powder diffraction peaks were measured with a General Electric XRD5 diffractometer using Ni-filtered $Cu K_\alpha$ radiation. The intensities are expressed relative to the intensity of the strongest line (311), which was re-measured each time in order to eliminate the effects of long-term instrument drift. Where two or more peaks could not be resolved, their intensities are grouped under a single intensity.

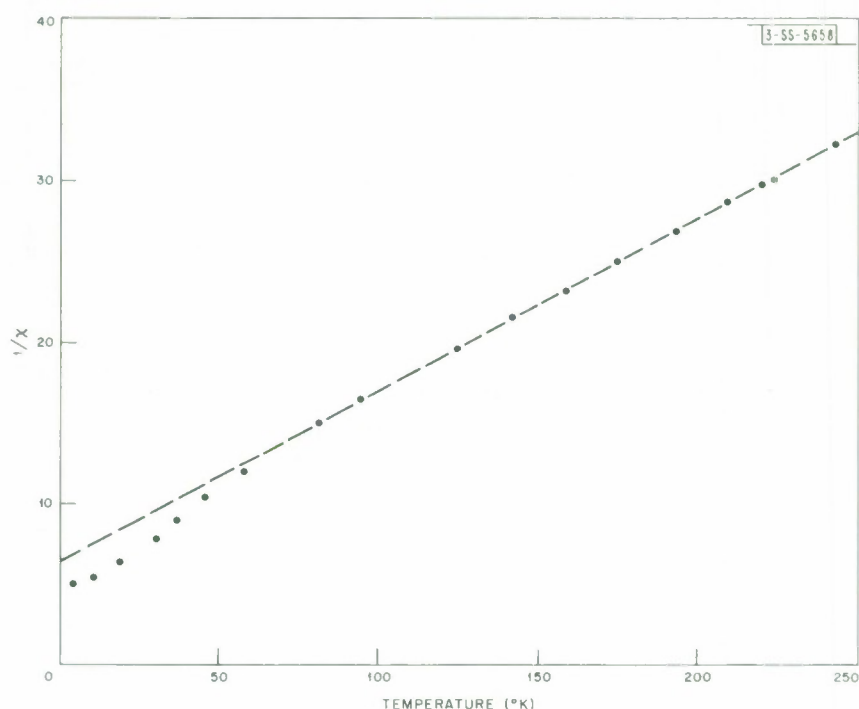


Fig. III-6. Reciprocal magnetic susceptibility ($1/\chi$) vs temperature for MnYb_2S_4 .

The structural parameters were refined by using a computer program¹⁶ which adjusts all parameters including site occupancy to obtain a minimum value for the factor R , defined as $100\sum |I_{\text{obs}} - I_{\text{calc}}| / \sum I_{\text{calc}}$. The observed and calculated intensities obtained by applying this program are compared in Table III-2. The final refinement gave $R = 8.2$, a U parameter for the sulfur position of 0.380 ± 0.002 , and the temperature factors $B_{\text{Mn}} = 0.0$, $B_{\text{Yb}} = 0.5$, and $B_{\text{S}} = 0.1$. The Mn atoms occupy the tetrahedral positions, and the Yb atoms occupy the octahedral positions in the spinel structure.

In an attempt to improve the agreement between calculated and observed intensities, the calculations were repeated (1) allowing the concentration of Mn on octahedral sites and Yb on tetrahedral sites to vary, and (2) allowing the tetrahedral Mn atoms to fill the octahedral vacancies in the spinel structure. The agreement was not improved in either case. The relatively large value of R may be due to the deterioration of the sample surface because of attack by the atmosphere.

The S atoms are the only atoms in the spinel structure whose positions may vary. For ideal close packing, their U parameter would be 0.375. The value of 0.380 measured for MnYb_2S_4 is lower than the values obtained for other Mn^{2+} spinels¹⁷ (e.g., MnIn_2S_4 , 0.384; MnCr_2S_4 , 0.386; MnAl_2O_4 , 0.390) because of the larger size of the Yb^{3+} ions compared with the other 3+ cations. (Patrie, Flahaut, and Domange¹⁴ found the U parameter for MnYb_2S_4 to be 0.375 ± 0.004 , but this value was obtained from the intensity ratios for only two sets of reflections, 311/333-511 and 531/731-533.)

J. M. Longo D. Batson
P. M. Raccach C. H. Anderson

TABLE III-2
OBSERVED VS CALCULATED X-RAY INTENSITIES FOR MnYb_2S_4
($a = 10.95$, U parameter = 0.380, $R = 8.2$)

(hkl)	I_{obs}	I_{calc}	(hkl)	I_{obs}	I_{calc}
111	64.2	64.3	555, 751, 662	14.8	15.2
220	8.9	5.7	840	17.0	16.2
311	100.0	100.0	753, 911	6.6	4.5
222	27.2	26.5	931	8.0	7.4
400	50.2	63.2	844, 755, 933, 771	23.6	22.2
331	16.2	15.8	862, 773		
422	4.9	2.5	951, 666	11.8	11.9
511, 333	44.2	41.0	10, 2, 0; 10, 2, 2		
440	63.4	69.6	953	2.9	2.4
531	15.8	15.9	775; 11, 1, 1	4.1	3.5
620	3.1	1.0	880, 955		
533, 622	24.8	25.3	11, 3, 1; 971	11.9	10.9
444	16.2	14.0	973; 11, 3, 3; 10, 6, 2	10.8	8.4
551, 711	9.0	8.2	884, 777		
642	2.0	1.2	12, 0, 0; 11, 5, 1	11.7	11.7
553, 731	19.2	20.4	975; 11, 5, 3	8.4	8.1
800	8.8	9.9	12, 4, 0; 991	15.9	15.9
733	2.3	1.4	11, 5, 5; 13, 1, 1		
822, 660	1.0	0.6	11, 7, 1; 10, 6, 6; 993	12.0	13.3
			12, 4, 4; 11, 7, 3		
			13, 3, 1; 977	11.6	14.4

REFERENCES

1. T.B. Reed, "Arc Techniques for Materials Research," to be published in Mater. Res. Bull. (March 1967).
2. M.H. Weatherly and J.E. Anderson, Electrochem. Tech. 3, 80 (1965).
3. Solid State Research Report, Lincoln Laboratory, M.I.T. (1966:3), p. 15, DDC 641498.
4. D.B. McWhan and M. Marezio, J. Chem. Phys. 45, 2508 (1966).
5. S. Minomura, B. Okai, H. Nagasaki, and S. Tanuma, Phys. Letters 21, 272 (1966).
6. Y. Kato and T. Ikezu, Phys. Letters (Amsterdam) 23, 644 (1966).
7. J.S. Kasper and H. Brandhorst, J. Chem. Phys. 41, 3768 (1964).
8. A. Jena, M.B. Bever, and M.D. Banus, Trans. Met. Soc. AIME (to be published).
9. J.N. Zemel, J.D. Jensen, and R.B. Schoolar, Phys. Rev. 140, A330 (1965).
10. E.G. Bylander, Mater. Sci. Eng. 1, 190 (1966).
11. J.M. Besson, *et al.*, Appl. Phys. Letters 7, 206 (1965), DDC 628560.
12. J.F. Butler, A.R. Calawa, and T.C. Harman, Appl. Phys. Letters (to be published).
13. J.O. Dimmock, I. Melngailis, and A.J. Strauss, Phys. Rev. Letters 16, 1193 (1966), DDC 642225.
14. M. Patrie, J. Flahaut, and L. Domange, C.R. Acad. Sci. 258, 2585 (1964).
15. S. Kern and P.M. Raccah, J. Phys. Chem. Solids 26, 1625 (1965), DDC 624722.
16. P.M. Raccah and J.B. Goodenough, Phys. Rev. (to be published).
17. P.M. Raccah, R.J. Bouchard, and A. Wold, J. Appl. Phys. 37, 1436 (1966), DDC 641000; R.W.G. Wyckoff, Crystal Structures (Interscience, New York, 1965), 2nd ed., Vol. 3, p. 78.

IV. PHYSICS OF SOLIDS

A. ELECTRONIC BAND STRUCTURE

1. Exciton Fine Structure in Interband Magnetoabsorption of InSb

We have observed exciton fine structure in the interband magnetoabsorption spectrum of InSb. This structure can be used to estimate the exciton contributions to the energy level separations deduced from the interband magnetoabsorption and to check existing theories for exciton levels in high magnetic fields. By going to a lower temperature, much sharper absorption lines were obtained than observed previously. The two lowest energy absorption bands observed with $E \parallel H$ and propagation transverse to the field involve the lowest spin-up and spin-down conduction band Landau levels, respectively. Three components were resolved in each of these bands. From the symmetric line shape, it was deduced that the two components at lower energy are associated with discrete exciton levels. The component at higher energy is relatively weak and appears as an edge, with absorption dropping off slowly on the high energy side; this behavior is characteristic of the exciton continuum as predicted by Elliott and Loudon.¹ Only the lowest exciton peak can be seen at low magnetic fields, where its energy appears to be quadratic with H . The separation between the lowest exciton peak and the edge agrees closely with theory for magnetic fields up to 40 kG. The location of the exciton peaks of intermediate energy are not accounted for by the theory of Elliott and Loudon, and are probably associated with forbidden transitions involving additional valence band levels.

E. J. Johnson

2. Magneto-Optical Studies on Vapor Transport Grown GaSe at 1.5°K

During this quarterly period, we have been examining samples of vapor transport grown GaSe.[†] The spectrum obtained from these crystals is appreciably different from that observed in melt grown material. A photographic print of the absorption spectrum for a 3.7- μ thick vapor transport grown sample is shown in Fig. IV-1. This was taken in the Faraday geometry at 1.5°K and at fields up to 93.5 kG. At the lower fields, more than a dozen Landau transitions can be seen. At higher fields, a new series of lines that fall between the lines of the main series is observed. Representative densitometer traces of the spectra shown in Fig. IV-1 are presented in Fig. IV-2. The absorption coefficient $\alpha(H)$ for this material is approximately three times larger at the peaks than has been previously observed. We attribute this to the total absence of strain in the sample. With the application of a magnetic field, the density of states coalesces right at the Landau levels rather than smearing out around them; thus, for the first time, magneto-absorption oscillations of the direct transition appear on transmission as sharp spikes rather than the previously observed damped sinusoidal-like oscillations.

The second series first appears between 25 to 30 kG. The ratio of the absorption of the peaks of the second series to that of the first for a given field increases approximately linearly with

[†] We are grateful to E. Mooser of the Cyanamid European Research Institute, Geneva, for making this material available to us.

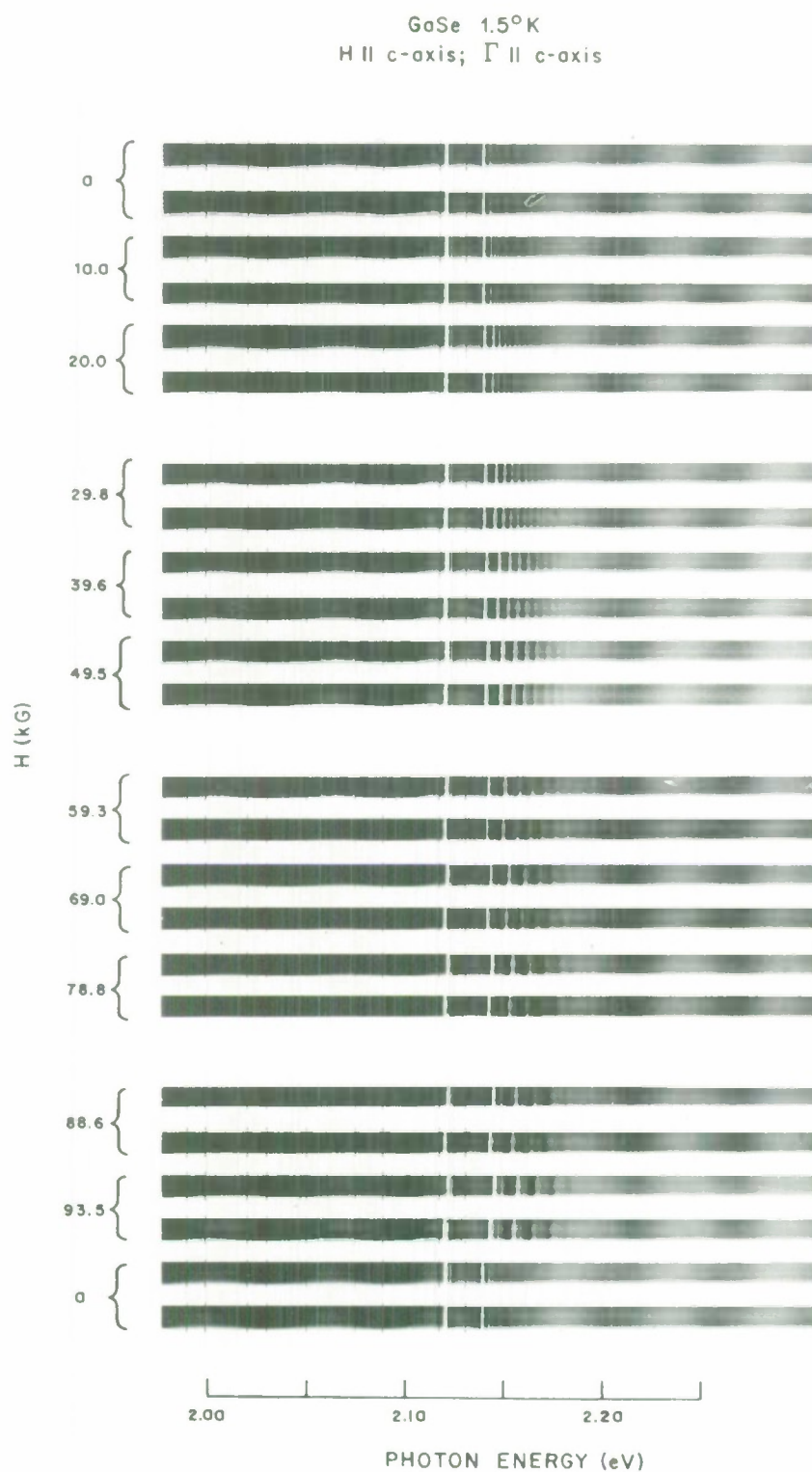


Fig. IV-1. Photographic print of absorption spectrum of vapor transport grown GaSe in Faraday geometry at 1.5°K. Alternate exposures are for right and left circularly polarized light, respectively.

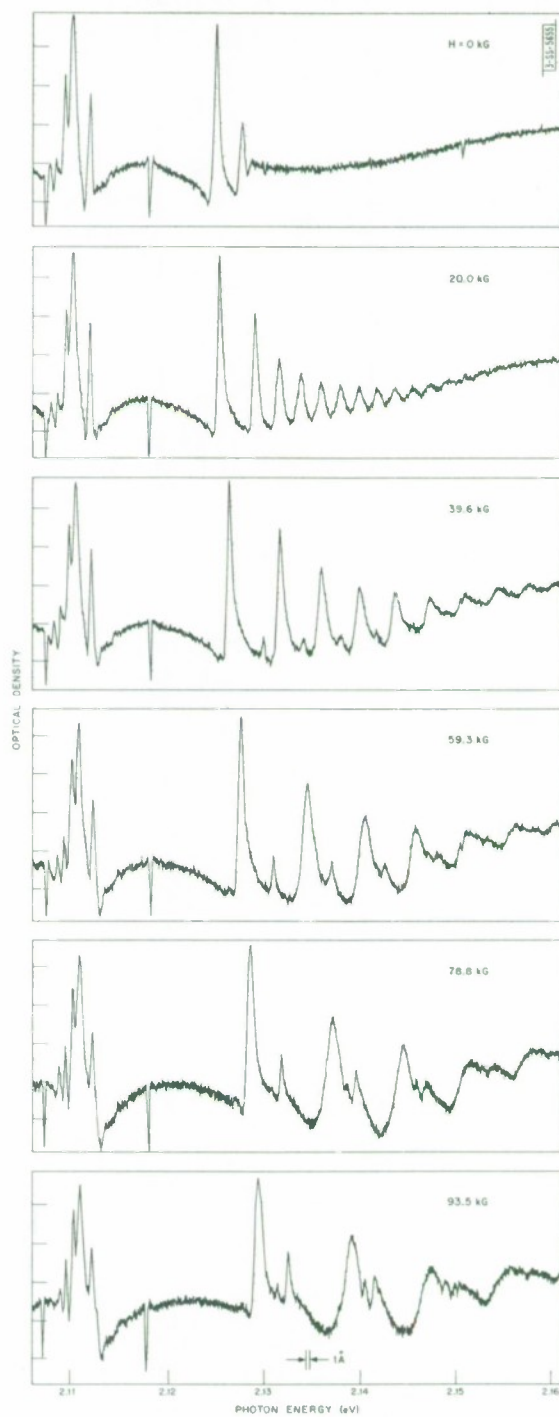


Fig. IV-2. Densitometer traces of representative spectra of Fig. IV-1 for unstrained GaSe. All traces shown here are for right circularly polarized radiation. Ordinates are in units of optical density, hence they are proportional to absorption coefficient (one division $\sim 500 \text{ cm}^{-1}$).

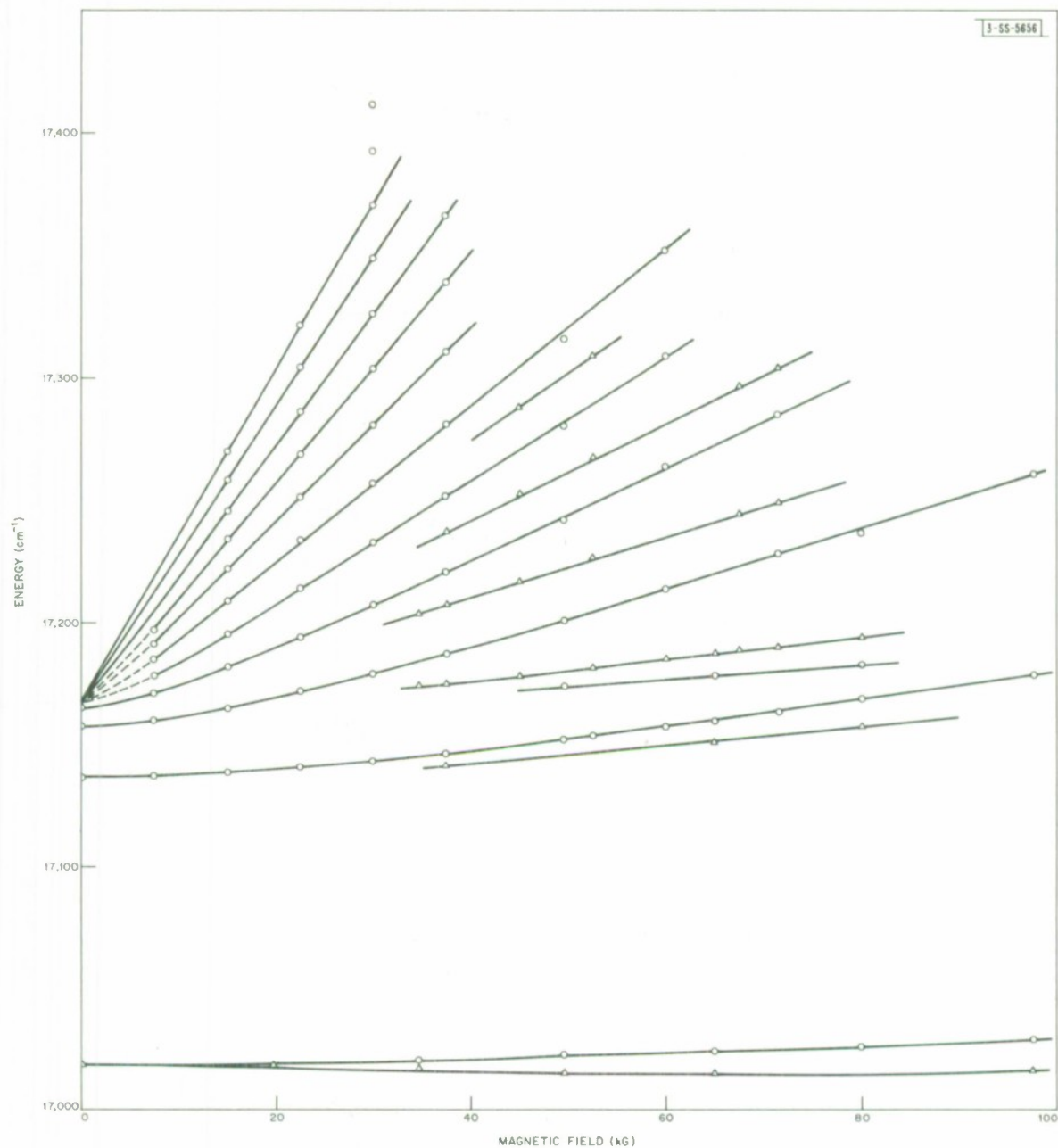


Fig. IV-3. Positions of magnetoabsorption direct transitions in unstrained GoSe as function of magnetic field for Faraday geometry. Lowest three transitions have been indicated for both left and right circularly polarized light; for clarity, higher energy transitions have been shown for right circularly polarized light only.

magnetic field. In the limit of $H = 0$, this new series converges for higher magnetic quantum numbers to the same edge energy (within ± 0.5 meV) as does the previously observed² main series, both of which are shown in the fan chart in Fig. IV-3. This fact and the similarity in the line-shapes of the two series suggest that the two series correspond to transitions at the same position in the Brillouin zone (the Γ -point). The second series has a transverse reduced effective mass of $\sim 0.13 m$ and a linear Zeeman splitting corresponding to a g -factor $g_{hz} - g_{ez} \sim -3.0$. There are several interpretations that are not incompatible with the present experimental data, all of which lead to the conclusion that one of the band edges at the energy gap is a complex band. Most probably, the valence band is doubly degenerate. (The point group of GaSe is D_{3h} , which has two-dimensional representations at the Γ -point.) That the transverse reduced mass for the second series is approximately equal to that for the first series leads to the following two most likely possibilities: (a) both hole masses are large and the two series correspond to $\Delta n = 0$ transitions from each of the hole ladders, or (b) the lighter hole mass is approximately 2 to 3 times the electron mass and one obtains a set of transitions for some value $\Delta n \neq 0$ in addition to the allowed transition. This second model is consistent with transport data obtained by Brebner³ for holes in GaSe. As can be seen in Fig. IV-2, a third series appears at fields > 60 kG; this series is now being studied in detail.

J. Halpern

3. Interband Magnetoreflexion and Band Structure of HgTe[†]

The analysis of HgTe interband magnetoreflexion data⁴ by the coupled $\Gamma_6 - \Gamma_7 - \Gamma_8$ theory⁵ has been completed. The $\Gamma_6 \rightarrow \Gamma_8$ transitions are observed only up to photon energies which correspond to initial and final states 0.05 eV, or less, into the Γ_6 valence band and Γ_8 conduction band. These transition energies agree well with those predicted by the theory. With higher band parameters which are about the same as those of germanium and InSb, we have made a two-parameter least-squares fit and find $E_g \equiv E(\Gamma_6) - E(\Gamma_8) = -0.283 \pm 0.001$ eV, and $E_p = 18.1 \pm 1.0$ eV, where E_p is proportional to the square of the momentum matrix element between Γ_6 and Γ_8 states. The stated uncertainties on the best-fit parameters are several times those which occur when the higher band parameters are varied over a range generated by their values in germanium, InSb and gray tin.

Since transitions between Γ_8 bands extend more than 0.2 eV into the Γ_8 conduction bands, the theory of Ref. 5 is not adequate to give a close fit; this theory includes the $\Gamma_8 - \Gamma_{15}$ (higher conduction band) $\vec{k} \cdot \vec{p}$ interaction only to order k^2 . For transitions above 0.1 eV in the Γ_8 conduction band (which are observed in our experiment), higher order contributions are important. The zero magnetic field theories of Fawcett,⁶ and of Cardona and Pollak,⁷ applied to germanium, treat this $\vec{k} \cdot \vec{p}$ interaction exactly and give 10-percent corrections to the k^2 theory at energies of 0.1 to 0.2 eV into the Γ_8 bands. A correction of this size would therefore be expected for HgTe and is of the proper sign to greatly improve the fit between experiment and theory.

We have not been able to obtain information on the size of the inversion asymmetric terms, partly because they are not included in our theory. Theoretical work which has treated them has been applied only to InSb (Ref. 8), and the computational results are too specific to be useful to us. We hope that a comparison of the $\Gamma_8 \rightarrow \Gamma_8$ transitions in HgTe and gray tin will give experimental evidence of the size of these terms in HgTe.

[†] This experiment was carried out using the high field facilities of the National Magnet Laboratory, M.I.T.

Section IV

E_g and E_p , found from the $\Gamma_6 \rightarrow \Gamma_8$ transition data, have been used to calculate the variation of effective mass m^* with concentration n for the Γ_8 conduction band. This result is in good agreement with determinations from the Shubnikov-de Haas effect, intraband reflection, intraband magnetoreflexion, and high magnetic field thermoelectric power measurements, except at concentrations greater than $1 \times 10^{18} \text{ cm}^{-3}$ where the higher band terms, of order greater than k^2 , make a measurable contribution. Some of the m^* vs n data have been used in the past by several authors to obtain $E_g \approx -0.15 \text{ eV}$ and $E_p \approx 14 \text{ eV}$. There are two reasons why these analyses gave quite different results from the direct interband magnetoreflexion measurement: first, the scatter in the m^* vs n data is very large; second, at high concentration values, the considerable contribution from higher band terms of order greater than k^2 (and also all higher band terms) was neglected. The higher band contributions are much more important for materials such as gray tin and HgTe with a Γ_8 conduction band than for materials such as InSb with a Γ_6 conduction band.

A more detailed description of these results is being submitted for publication.

S. H. Groves
R. N. Brown†
C. R. Pidgeon†

4. Magnetoreflexion Experiments in Arsenic

Study of the magnetoreflexivity of arsenic is continuing. The oscillations observed with the magnetic field parallel to the binary axis were found to arise from transitions between a pair of bands with an energy gap of $0.346 \pm 0.002 \text{ eV}$ and a reduced effective cyclotron mass, near the bottom of the band, of $0.023 m_0$. At higher energies, the dispersion relations of the bands involved in the transitions become significantly nonparabolic.

Magnetoreflexivity oscillations with the field parallel to the bisectrix axis have also been observed. The data were quite similar to that found for the binary face. With an improvement in the spectral resolution, we were able to observe the lowest quantum oscillation and found that the amplitude of this oscillation went abruptly to zero at 0.360 eV , which is 0.014 eV above the energy gap. This definitely indicates the presence of a small pocket of carriers associated with one of the bands involved in this transition. The number of carriers in the new pocket is too small to significantly affect the equality condition between the number of holes and electrons, which is required of a semimetal. Also, the de Haas-van Alphen period will be very long, which may explain why no de Haas-van Alphen oscillations associated with this carrier have yet been found.⁹

It was determined that the magnetoreflexivity oscillations disappeared when the light was polarized perpendicular to the trigonal axis. The only points in the Brillouin zone which have bands of the proper symmetry to give rise to such optical selection rules lie among the trigonal axis. The similarity of the binary and bisectrix data is also consistent with this conclusion. However, our findings are in direct contradiction with the Lin-Falicov model for arsenic,¹⁰ which places no carriers along the trigonal axis of the Brillouin zone.

† National Magnet Laboratory, M.I.T.

On the other hand, the magnetorefectivity oscillations previously reported for the magnetic field perpendicular to the trigonal face are predicted by the Lin-Falicov band model as arising from transitions across a gap produced by the spin-orbit splitting of a crossover degeneracy along the Q or twofold axis. At present, further tests for the validity of this band model are being carried out by Dr. S. Iwasa at the National Magnet Laboratory, using high resolution laser spectroscopy.

M. S. Maltz[†]
Mildred S. Dresselhaus

5. Fourier Expansion of Phonon Dispersion Relations for Silicon and Germanium

The Fourier expansion technique, previously used to calculate the electronic energy bands and dielectric constant of silicon and germanium,¹¹ has now been applied to the lattice vibration spectrum for solids which crystallize in the diamond structure. There are three acoustic and three optical branches in the phonon problem. The Fourier expansion of the equations of motion for these phonons is of precisely the same form as that for the coupled bonding and antibonding p-bands of the electron problem. Whereas the eigenvalue of the effective mass Hamiltonian for the electron problem yields the dispersion relation directly, the eigenvalue of the phonon problem is $[\omega(k)]^2$, the square of the phonon frequency.

The determination of the band parameters or Fourier expansion coefficients for the phonon problem is very simply accomplished because of the large quantity of available experimental information. These parameters are evaluated explicitly to third nearest-neighbor terms for silicon and germanium using experimental measurements of the elastic constants and of the vibrational spectrum as obtained by neutron diffraction.^{12,13}

The force constant model, which has previously been used to express the dispersion relations for phonons in these materials,¹⁴ is of the same form as the Fourier expansion. The major advantage of the Fourier expansion point of view is that one need not be restricted to any particular model, but only to the crystal symmetry. This flexibility makes it possible to include interactions to distant neighbors, thereby obtaining dispersion curves which are in better agreement with the experimental data, particularly with regard to the curvature of the branches.

G. F. Dresselhaus
Mildred S. Dresselhaus

B. MAGNETISM

1. NMR in Ferromagnetic Semiconductor CdCr_2Se_4

We have observed the zero field Cr^{53} nuclear resonance in the ferromagnetic state of the spinel CdCr_2Se_4 . At 4.2°K, the resonance occurs at the relatively low frequency of 44.54 MHz, which indicates considerable covalency and is consistent with the semiconducting behavior of this compound. The resonance is split by quadrupole interactions into a triplet of sharp lines with widths of 30 kHz or less, and with a total temperature-independent separation of 1.8 MHz. Quadrupole splitting appears inconsistent with the reported positive sign for the cubic anisotropy

[†] Department of Electrical Engineering, M.I.T.

Section IV

constant K_1 (Ref. 15). The resonance signal was followed from helium temperatures to 115°K ($0.9 T_c$) with a super-regenerative spectrometer. Spin-echo measurements show that the loss of signal above 115°K can be attributed to a rapid increase in the nuclear relaxation rate with temperature. As a function of temperature, the hyperfine field decreases much more rapidly than the magnetization predicted by molecular field theory and somewhat more rapidly than the previously measured magnetization.¹⁶

Between liquid helium and liquid nitrogen temperatures, the hyperfine field shows a surprisingly linear decrease with temperature. If we assume, as is normally done, that the hyperfine field H_{hyp} is proportional to the magnetization as described by $H_{\text{hyp}} = A I_{\text{nuc}} \cdot \langle S \rangle_{\text{el}}$, then the linear temperature-dependent term in the magnetization dominates any higher power term at low temperatures. This would be contrary to the expected $T^{3/2}$ and higher power terms expected from simple spin wave theory. The explanation may lie in a more realistic spin wave calculation, taking into account the large number of magnetic interactions or, alternatively, there may be a large temperature dependence of the hyperfine constant A . The value of A depends on the covalency of the chromium ions with selenium; since the band structure in this compound, as determined from optical data, changes rapidly with temperature, the observed difference between the hyperfine field and magnetization may be caused by the change in covalency.

M. Rubinstein[†] J. Feinleib
G. H. Stauss[†] A. Wold[‡]

2. High-Temperature Expansion of Spin Correlation Function for Classical Heisenberg Model

The following is an abstract of a paper which is being submitted for publication and will constitute part of a Ph.D. thesis to be submitted to the Department of Physics, Harvard University.

"The diagrammatic representation of the first nine coefficients for loose-packed lattices and the first eight coefficients for close-packed lattices in a high-temperature series expansion of the zero-field spin correlation function $\langle S_f \cdot S_g \rangle_\beta$ is presented. This calculation exploits the order-of-magnitude simplifications which occur in treating the quantum-mechanical spin operators in the Heisenberg model as isotropically-interacting classical vectors of length $[S(S+1)]^{1/2}$. This semiclassical approximation – the "classical" Heisenberg model – appears to be excellent for some critical properties of interest if $S > 1/2$. A recursion relation is seen to obviate the need to consider the sizable classes of disconnected diagrams and diagrams containing articulation points. The utility of the high-temperature series for $\langle S_f \cdot S_g \rangle_\beta$ is discussed. It contains information – relevant to current experiments – not contained in the high-temperature expansions for the thermodynamic functions (e.g., susceptibility, specific heat), as well as providing an efficient method of extending the series for all the thermodynamic functions together. As an example of the applicability of the series expansion of $\langle S_f \cdot S_g \rangle_\beta$ to obtain information concerning the short-range magnetic order to be

[†] U.S. Naval Research Laboratory, Washington, D.C.

[‡] Brown University, Providence, Rhode Island.

expected for $T > T_c$, a calculation of the elastic paramagnetic neutron scattering cross section for normal cubic spinels with nearest-neighbor A-B exchange interactions is given, and contact is made with the experiments on MnCr_2O_4 ."

H. E. Stanley

C. SCATTERING EXPERIMENTS WITH LASERS

1. Resonant Stimulated Raman Scattering

We have observed Raman scattering in quartz at low temperatures ($\sim 20^\circ\text{K}$) in which the Stokes line is split into two or three sharp components. The splitting, of the order of 0.2 cm^{-1} , was measured precisely on a Fabry-Perot etalon; it corresponded to the resonant frequency of the quartz sample cavity, which had plane, parallel end faces. The interesting aspect of this observation is that the calculated refractive index of the sample is approximately 10 to 20 percent larger than the usual index for quartz.

The splitting scales approximately with change in sample length; furthermore, the second Stokes line is also seen occasionally to be split into similar components. The spontaneous Raman line is, of course, many wavenumbers wide and can thus support a number of cavity modes near its peak. The increase in refractive index is presumably due to the nonlinear response of the material under high electric field intensity; however, the effect seems to depend on the focal length of the lens used to focus the beam into the sample. The dependence of the splitting as a function of incident laser power is now under investigation.

P. E. Tannenwald
F. H. Perry

2. Raman Spectra of Trigonal, α -Monoclinic, and Amorphous Selenium

We have measured the Raman spectra of three modifications of selenium at room temperature using a YAG:Nd^{3+} laser. The first-order Raman spectrum of trigonal selenium consists of three strong lines. We have identified the mode symmetry by polarization measurements shown in Fig. IV-4. The second-order spectrum shown in Fig. IV-5 can be explained in terms of two-phonon transitions. The assignment of modes in the Raman spectra of α -monoclinic (Fig. IV-6) and amorphous (Fig. IV-7) selenium is discussed in detail in a forthcoming publication.¹⁷

A. Mooradian
G. B. Wright

Section IV

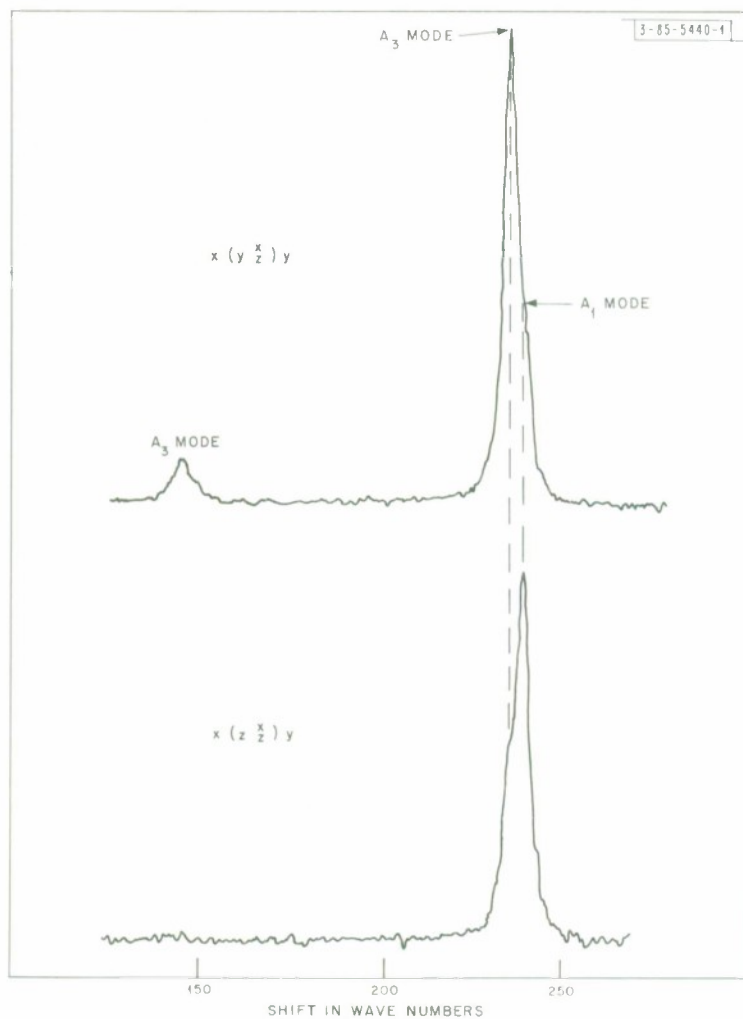


Fig. IV-4. Polarized light Raman spectrum of trigonal selenium. In symbol $a(bc)d$, a and d give direction of propagation of incident and scattered light relative to crystal axes, while b and c give direction of propagation of incident and scattered light.

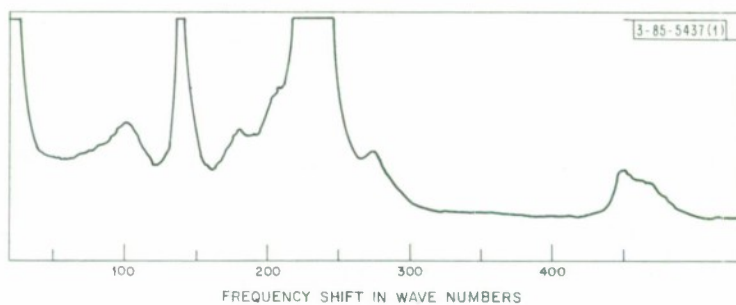


Fig.IV-5. Second-order Raman spectrum of trigonal selenium.

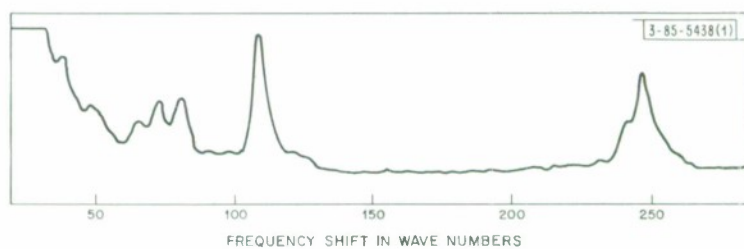


Fig.IV-6. Raman spectrum of α -monoclinic selenium.

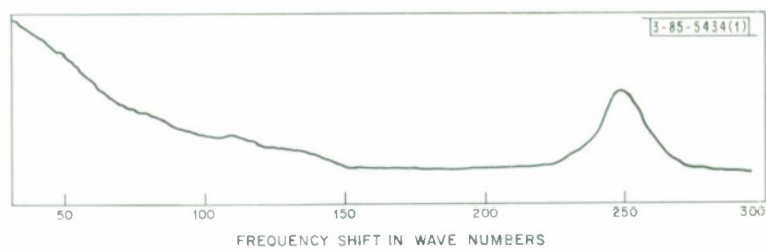


Fig.IV-7. Raman spectrum of omorphaus selenium.

REFERENCES

1. R.J. Elliott and R. Loudon, J. Phys. Chem. Solids 15, 196 (1960).
2. J. Halpern, Proceedings of the International Conference on the Physics of Semiconductors, Kyoto, Japan, 1966, in J. Phys. Soc. Japan Suppl. 21, 180 (1966).
3. J.L. Brebner, private communication.
4. R.N. Brown and S.H. Groves, Bull. Am. Phys. Soc. 11, 206 (1966); Solid State Research Report, Lincoln Laboratory, M.I.T. (1966:1), p.37, DDC 632998, H-721.
5. C.R. Pidgeon and R.N. Brown, Phys. Rev. 146, 575 (1966).
6. W. Fawcett, Proc. Roy. Soc. (London) 85, 931 (1965).
7. M. Cardona and F.H. Pollak, Phys. Rev. 142, 530 (1966).
8. R.L. Bell and K.T. Rogers, Phys. Rev. 152, 746 (1966).
9. M.G. Priestley, L. Windmiller, J.B. Ketterson, and Y. Eckstein (to be published).
10. P.J. Lin and L.M. Falicov, Phys. Rev. 142, 441 (1966).
11. G. Dresselhaus and M.S. Dresselhaus (to be published).
12. B.N. Brockhouse and P.K. Iyengar, Phys. Rev. 111, 747 (1958).
13. B.N. Brockhouse, Phys. Rev. Letters 2, 256 (1959).
14. H.M.J. Smith, Trans. Roy. Soc. (London) 241, 105 (1948).
15. R.C. LeCraw, H. Von Phillipsborn, and M.D. Sturge (to be published).
16. N. Menyuk, K. Dwight, R.J. Arnett, and A. Wold, J. Appl. Phys. 37, 1387 (1966), DDC 642203.
17. G. Lucovsky, et al., Solid State Commun. (to be published).

DOCUMENT CONTROL DATA - R&D

(Security classification of title, body of abstract and indexing annotation must be entered when the overall report is classified)

1. ORIGINATING ACTIVITY (Corporate author) Lincoln Laboratory, M.I.T.		2a. REPORT SECURITY CLASSIFICATION Unclassified	
		2b. GROUP None	
3. REPORT TITLE Solid State Research			
4. DESCRIPTIVE NOTES (Type of report and inclusive dates) Quarterly Technical Summary - 1 November 1966 through 31 January 1967			
5. AUTHOR(S) (Last name, first name, initial) McWhorter, Alan L.			
6. REPORT DATE 15 February 1967		7a. TOTAL NO. OF PAGES 64	7b. NO. OF REFS 81
8a. CONTRACT OR GRANT NO. AF 19(628)-5167		9a. ORIGINATOR'S REPORT NUMBER(S) Solid State Research (1967:1)	
b. PROJECT NO. 649L		9b. OTHER REPORT NO(S) (Any other numbers that may be assigned this report) ESD-TR-67-162	
c.			
d.			
10. AVAILABILITY/LIMITATION NOTICES Distribution of this document is unlimited.			
11. SUPPLEMENTARY NOTES None		12. SPONSORING MILITARY ACTIVITY Air Force Systems Command, USAF	
13. ABSTRACT This report covers in detail the solid state research work at Lincoln Laboratory for the period 1 November 1966 through 31 January 1967. The topics covered are Solid State Device Research, Optical Techniques and Devices, Materials Research, and Physics of Solids.			
14. KEY WORDS			
solid state devices	laser research	magnetoabsorption	magnetoplasma
electron beam pumping	materials research	vapor growth	stimulated Raman
infrared	arc melting	magnetoreflexion	scattering
optical techniques	electronic band	Fourier expansion	magnetism
and devices	structure	phonons	